4 Evaluation of Causes and Mechanisms of Irradiation-Assisted Cracking of Austenitic Stainless Steel in PWRs (H. M. Chung and W. K. Soppet)

4.1 Introduction

Field failures have been reported in various PWR core internal components fabricated from austenitic SSs, such as baffle bolts, control rod cladding, pins, keys, and bolts. Many of the failed components were fabricated from cold-worked materials of Type 316, 347, and 304 SS. Typically, failures of PWR core internals are intergranular (IG) and are observed at neutron-damage levels approximately a few orders of magnitude higher (i.e., >10 dpa) than the threshold damage level of BWR core internals (i.e., ≈0.7 dpa). At this time, the database and mechanistic understanding of PWR core internals are very limited, and it is not clear if the failures should be classified as irradiation–assisted stress corrosion cracking (IASCC) or irradiation–assisted cracking (IAC); the latter does not require an aqueous environment and would occur even in air.

The objectives in this task are to evaluate the susceptibility of austenitic SS core internals to IAC in PWRs as a function of the fluence, water chemistry, material chemistry, and cold work. The program will focus on the following: (a) evaluation of the effects of PWR-like high fluence on susceptibility to IASCC, (b) neutron irradiation embrittlement, e.g., loss of fracture toughness, (c) void swelling behavior in austenitic SSs, (d) effect of cold work and solution anneal, (e) fracture toughness and SCC behavior of cast duplex SSs at high fluence, and (f) effectiveness of mitigative measures, such as optimization of ferrite content, grain-boundary engineering, and minimization of S concentration. Tests will be conducted on austenitic SS specimens irradiated in the BOR–60 reactor in Russia.

4.2 Irradiation of Austenitic Stainless Steels in the BOR-60 Reactor

An experiment has been initiated to irradiate specimens of various types of materials and geometry under PWR-like conditions. The irradiation experiment is being conducted in cooperation with the Cooperative Irradiation-Assisted Stress Corrosion Cracking Research (CIR) Program. Irradiation of the specimens is performed in the BOR-60 Reactor, a sodium-cooled breeder reactor located in the Research Institute of Atomic Reactors (RIAR), Dimitrovgrad, Ulyansk Region, Russian Federation.

In the first part of the irradiation campaign, specimens were irradiated to ≈5 and ≈10 dpa in Irradiation Cycle BORIS-6 in flowing sodium maintained at 322.1-322.6°C. Further irradiation of specimens to ≈40 dpa in Irradiation Cycle BORIS-7 continued in the second part of the campaign. After irradiation in BORIS–6, 48 tensile specimens (contained in 12 bundles) and 166 disk specimens (contained in 4 capsules) were discharged. Each bundle contains 4 tensile specimens, and the disk capsules contain 23-56 disk specimens. The specimens have been transported to the Westinghouse hot cell through Studsvik. Westinghouse is performing the work to separate and repackage ANL specimens from the CIR specimens. The ANL specimens are expected in August 2004.

Tests performed on materials irradiated to lesser damage levels in the Halden BWR reactor, however, give some insight into potential mechanisms for IASCC that is also relevant to PWRs. Selected specimens irradiated in the Halden reactor or in commercial BWRs were fractured in inert environments after SSRT testing in water or after charging with hydrogen. The purpose of the study was to perform relatively low–cost fracture tests that could provide insights helpful to understand the mechanism of PWR IASCC. Needle–like specimens were prepared from selected BWR neutron absorber tubes and a control

blade sheath. After cathodically charging with hydrogen the specimens were fractured at 23°C in the vacuum environment of an Auger electron microscope. The significant results are summarized below.

4.3 Representation of IASCC–Resistant or –Susceptible Behavior of Types 304 and 316 Stainless Steel in Sulfur–Carbon Map

After exposure to the conditions of the SSRT test in BWR water, susceptibility to IG cracking in inert environment was determined by rapid bending in air at 23°C. Similar tests were also performed on hydrogen–charged specimens in vacuum. Both types of bend fracture exhibited similar characteristics, suggesting that in both cases the failures occurred due to hydrogen-induced IG failure. However, steels that showed high susceptibility to IGSCC in 289°C water exhibited low susceptibility to IG cracking in the tests at 23°C air or vacuum, and vice versa. This finding indicates that although IG cracking in 23°C is dominated by H–induced embrittlement of ordinary grain boundaries, other processes control IASCC in 289°C water.

On the basis of this investigation, and studies on binary Ni–S and crack-tip microstructural characteristics of LWR core internal components reported in the literature, an initial IASCC model based on a crack–tip grain–boundary process that involves S has been proposed. In this model, several processes play a key role: i.e., grain-boundary segregation of Ni and S, formation of grain-boundary oxide in front of the crack tip, formation of Ni– and S–rich thin films, and islands between the oxide and metal matrix, and disorder–induced melting or amorphization of the Ni–S thin films and islands at sufficiently high concentration of S.

Figure 59 is a two–dimensional map as a function of bulk S and C concentration[20–22,39,75–76] that shows the regimes in which austenitic SSs are found to be resistant or susceptible to IASCC in the PWR environment. The trends in Fig. 59 are similar to those observed earlier in the S–C map that shows the IASCC–resistant or –susceptible regimes under BWR oxidizing conditions (Fig. 21).

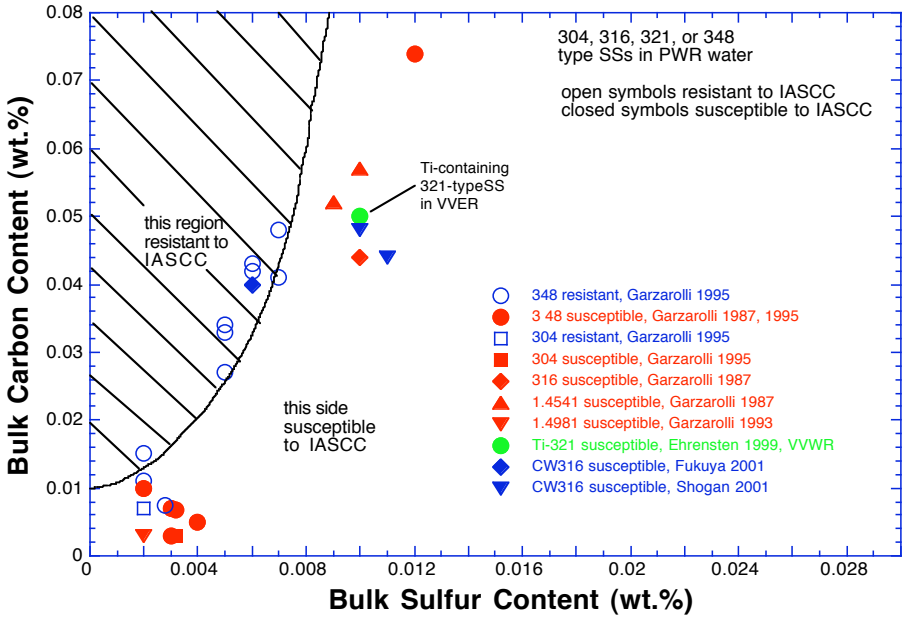

Figure 59. Representation of IASCC resistance or susceptibility of austenitic stainless steels as function of bulk S and C contents. Data obtained from PWR– or VVER—irradiated specimens in PWR, VVER, or PWR–like water reported in 1987–2004.

The beneficial effect of C can be explained based on the postulation that C atoms are dissolved in significant amount within the Ni– and S–rich thin film (thickness ≈3–8 nm) that was observed in some studies at the boundary between the steel matrix and Fe–Cr spinel oxide at a crack–tip grain boundary. In an initial model described in a previous annual report, it was assumed that such a Ni– and S–rich thin film loses metallic strength when the S content in the film exceeds a threshold level. Such loss of metallic strength is attributed to severe localization of free electrons in the Ni– and S–rich film when S content exceeds the threshold level. Without free electrons, the film no longer exhibits metallic behavior. A simple consideration suggests that C atoms can easily occupy the same octahedral sites in the unit cell of Ni sulfide that are normally occupied by S atoms. That is, when C concentration is high near the Ni– and S–rich thin film produced at the crack–tip grain boundary, S and C atoms compete to occupy the same octahedral sites of the unit cell of the film. Under such a situation, C dissolved in the film is expected to suppress the deleterious effect of S, which reduces the number of free electrons in the film, as discussed in Section 3.1.4.

5 Cracking of Nickel Alloys and Welds (B. Alexandreanu, O. K. Chopra, and W. J. Shack)

5.1 Introduction

This part of the study consists primarily of establishing CGRs under constant and cyclic loading and evaluating Ni alloys and weld metals metallographically to develop comprehensive and statistically significant analyses that could be used to determine the dependence of the SCC of these materials on alloy composition, microstructure, water chemistry, temperature, and other factors. The Ni–base alloys used as construction materials in light water reactors (LWRs) have experienced stress corrosion cracking (SCC). Primary–water SCC of Alloy 600 steam generator tubes in pressurized water reactors (PWRs) has been studied intensively.[77–79] Stress corrosion cracking has also occurred in Ni alloys used in applications such as instrument nozzles and heater thermal sleeves in the pressurizer[80] and penetrations for the control–rod drive mechanism (CRDM) in the reactor vessel closure heads.[81] In the fall of 1991, a leak was discovered in the pressure vessel head penetration at the Bugey 3 plant in France. Metallurgical evaluations indicated that the leak was caused by primary water SCC.[82] The main crack had initiated in Alloy 600 base metal and propagated into the Alloy 182 weld metal. Subsequent inspections of CRDM penetrations in domestic and foreign PWRs identified a small number of penetrations (<5% of the penetrations inspected) with axial cracks. None of the cracks were through–wall, and until recently, no more leaks occurred in pressure vessel head penetrations.

Leaks from axial through–wall cracks were identified at Oconee unit 1 in November 2000 and Arkansas Nuclear One unit 1 in February 2001.[83] During the next 15 months, inspections at Oconee units 2 and 3 and follow-up inspection at unit 1 identified both axial and circumferential cracks in reactor vessel head penetrations.[84] The presence of circumferential cracks, in particular, raised concerns regarding structural integrity.[85,86] Also, in October 2000, significant boron deposits were discovered near the Loop "A" reactor vessel nozzle to hot leg reactor coolant pipe weld at the V. C. Summer plant.[87] Ultrasonic inspection of the pipe revealed an axial crack and a short, intersecting circumferential crack, in the dissimilar metal weld at the top of the pipe. Earlier in 2000, two shallow axial flaws were found in the outlet nozzle–to–safe–end weld of Ringhals unit 3, and four axial indications were found in the same region of Ringhals unit 4, in Sweden.[88] Cracks have also been found in pressure vessel head penetrations at North Anna unit 2[89] and Davis-Besse nuclear power plant[90] and, more recently, in the bottom–mounted instrumentation nozzles at South Texas unit 1.[91,92]

Long–term operating experience indicates that although wrought Ni–base Alloy 600 is susceptible to SCC, the weld metal Alloys 82 and 182 used with Alloy 600 were perceived to be less susceptible. However, laboratory tests indicate that in PWR coolant environments, the SCC susceptibility of Alloy 182 may be greater than Alloy 600 and that of Alloy 82 may be comparable to Alloy 600. This apparent inconsistency between field and laboratory experience has been an issue that needs further investigation.

A program is being conducted at ANL to evaluate the resistance of Ni alloys and their welds to environmentally assisted cracking in simulated LWR coolant environments. The existing CGR data for Ni–alloys under cyclic and constant loads have also been analyzed to establish the effects of key parameters on CGRs; the results are presented elsewhere.[93–97] The fatigue crack growth data in air were analyzed to develop correlations for estimating the fatigue CGRs of Alloy 600 and 690 as a function of stress intensity factor range ΔK, load ratio R, and temperature.[98] The results indicate that in air, the CGRs of these materials are relatively insensitive to changes in frequency. The CGR (m/cycle) of Alloy 600 in air is best expressed as

$$da/dN = C_{A600} (1 - 0.82\ R)^{-2.2} (\Delta K)^{4.1}, \quad (11)$$

where ΔK is in $MPa \cdot m^{1/2}$, and the constant C_{A600} is given by a third-order polynomial of temperature T (°C) expressed as

$$C_{A600} = 4.835 \times 10^{-14} + (1.622 \times 10^{-16})T - (1.490 \times 10^{-18})T^2 + (4.355 \times 10^{-21})T^3. \quad (12)$$

In high–DO water, the CGRs of Alloy 600 show frequency–dependent enhancement under cyclic loading conditions. The environmental enhancement of growth rates does not appear to depend strongly on the material condition. In contrast, environmental enhancement of CGRs of Alloy 600 in low–DO water does seem to be strongly dependent on material conditions. In the literature[99–104] such variability has been attributed to parameters such as yield strength and grain boundary coverage of carbides, although the evidence for this dependence has been best demonstrated for steam generator tubing, rather than thicker structural materials.

In the earlier ANL work, correlations were developed to estimate the enhancement of CGRs in LWR environments relative to the CGRs in air under the same loading conditions. The best–fit curve for Alloy 600, either in the solution annealed (SA) condition or SA plus thermally treated condition, in ≈300 ppb DO water is given by the expression[95]

$$CGR_{env} = CGR_{air} + 4.4 \times 10^{-7} (CGR_{air})^{0.33}. \quad (13)$$

This section of the report presents CGR results for Alloy 600 from round robin tests and for Alloy 182 shielded metal arc (SMA) weld metal in simulated PWR environments at 320°C. The results have been compared with the existing CGR data for Ni–alloy welds to determine the relative susceptibility of the specific Ni–alloy weld to environmentally enhanced cracking under a variety of loading conditions. Detailed metallographic examinations of the material to characterize the microstructure of the weld metal are presented.

5.2 Experimental

5.2.1 Material and Specimen Design

Crack growth rate tests have been conducted on Alloy 182 weld metal samples in simulated PWR environments at 320°C in accordance with ASTM Designation E–647, "Standard Test Method for Measurement of Fatigue Crack Growth Rates." The tests were performed on 1–T compact tension (CT) specimens; the configuration of the CT specimen is shown in Fig. 60. Crack extensions were determined by the reversing DC potential drop technique. 14

The weld was prepared by welding two 152 x 305 mm (6 x 12 in.) pieces of 38–mm thick (1.5–in. thick) plate. The weld had a double "J" joint design and was produced by 48 weld passes. Root passes 1–5 were produced by gas tungsten arc (GTA) welding with Alloy 82 filler/electrode, and the other passes by shielded metal arc (SMA) process with Alloy 182 filler. The chemical compositions of the base and weld metals are given in Table 11. A schematic of the joint design and various passes is shown in Fig. 61 and the welding conditions for each weld pass are listed in Table 12. During welding the maximum inter–pass temperature was ≈120°C (250°F), and the weld surfaces were cleaned by use of a wire brush and grinding and by rinsing with de–mineralized water or alcohol. The orientation of the Alloy 182 SMA weld–metal specimen is shown in Fig. 62.

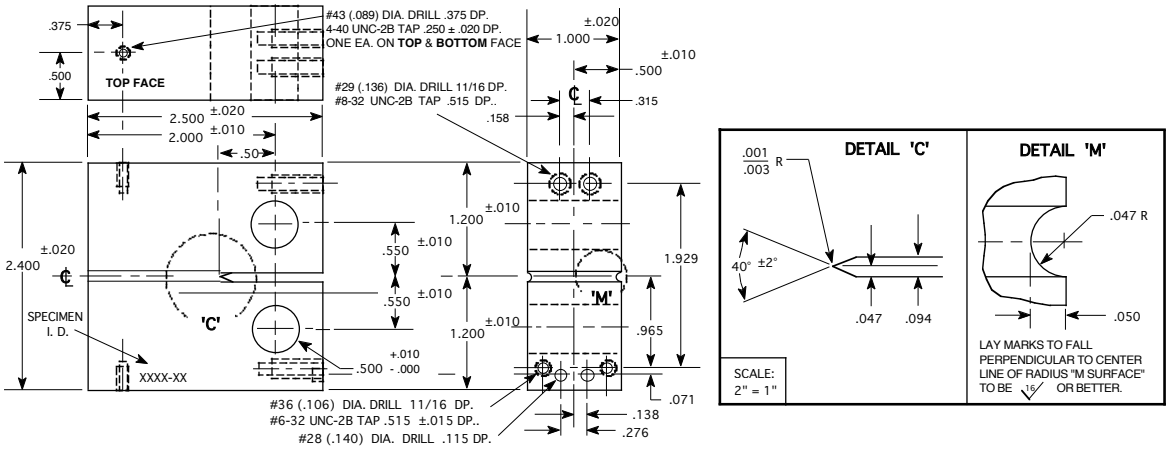

Figure 60. Configuration of compact-tension specimen used for this study (dimensions are in inches).

Table 11. Chemical composition (wt.%) of Alloy 600 base metal and Inconel 182 and 82 weld metals.

Alloy ID (Heat)	Analysis	C	Mn	Fe	S	P	Si	Cu	Ni	Cr	Ti	Nb	Co
Alloy 600													
(NX1310)	Vendor	0.07	0.22	7.39	0.002	0.006	0.12	0.05	76.00	15.55	0.24	0.07	0.058
	ANL	0.07	0.22	7.73	0.001	–	0.18	0.06	75.34	–	–	–	–
Alloy 182	Spec.	0.10	5.0–	6.0–	0.015		1.0	0.5		13.0–	1.0	1.0–	0.12 max
		max	9.5	10.0	max	–	max	max	Bal	17.0	max	2.5	
	ANL	0.05	6.97	6.82	0.005	0.008	0.56	0.01	69.22	–	–	1.70	–
Alloy 82	Spec.	0.10	2.5–	3.0	0.015		0.5	0.5	67.00	18.0–	0.75	2.0–	0.75 max
		max	3.5	max	max	–	max	max	min	22.0	max	3.0	

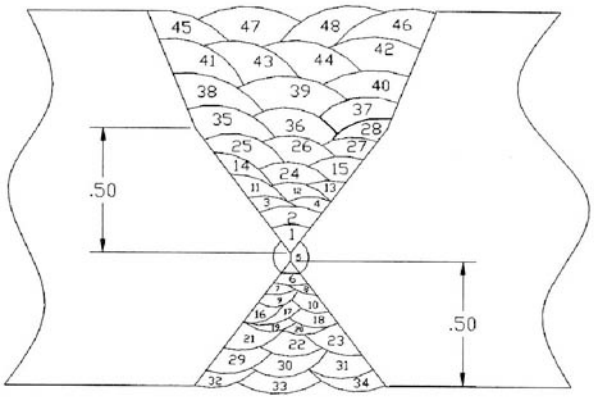

Figure 61. Schematic of the weld joint design and weld passes (dimensions are in inches).

Table 12. Welding process and conditions for various weld passes.

Weld Pass	Process	Filler Metal	Filler/Electrode Size	Current (A)	Voltage (V)	Travel Speed (in./min.)
1 – 5	GTA	Alloy 82	3/32	185 – 215	21 – 22	2 – 4
6 – 10	SMA	Alloy 182	3/32	140 – 155	24 – 26	6 – 7
11 –27	SMA	Alloy 182	1/8	155 – 170	25 – 27	6 – 7
28 – 48	SMA	Alloy 182	5/32	170 – 180	26 – 28	6 – 7

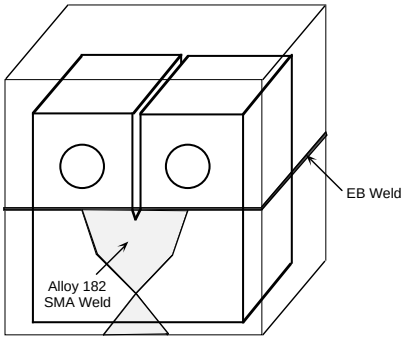

Figure 62. Orientation of the CT specimen from the Alloy 182 SMA weld.

5.2.2 Test Facility

The CGR tests were conducted with an MTS™ closed-loop electro–hydraulic material test system equipped with a Type 316 SS autoclave supplied with the test water solution from a feedwater tank. The simulated PWR feedwater contains less than 10 ppb DO, 2 ppm Li, 1000 ppm B, and ≈2 ppm dissolved hydrogen (≈23 cm^3/kg). It is prepared from the building deionized water by first passing this water through a local filtration system that includes a carbon filter, an Organex–Q filter, two ion exchangers, and a 0.2–mm capsule filter. The DO in the deionized water is reduced to <10 ppb by bubbling/sparging a mixture of N_2 + 5% H_2 through the water. A vacuum may be applied to the feedwater tank at the vent port, to speed deoxygenation. The PWR water is prepared by dissolving boric acid and lithium hydroxide in 20 L of deionized water before adding the solution to the supply tank. The hydrogen gas pressure of the feedwater tank was maintained at 34 kPa. The dissolved hydrogen in water was calculated from the tank hydrogen pressure and temperature.

Water samples are taken periodically to measure pH, resistivity, and DO concentration both upstream and downstream from the autoclave. An Orbisphere meter and CHEMetrics™ ampules are used to measure the DO concentrations in the supply and effluent water. The redox and open–circuit corrosion potentials were monitored at the autoclave outlet by measuring the ECPs of platinum and an Alloy 600 electrode, respectively, against a 0.1–M KCl/AgCl/Ag external (cold) reference electrode.

5.2.3 Test Procedure

The CGR tests were conducted in the load–control mode using a triangular, sawtooth, or trapezoidal waveform with load ratio R of 0.3–0.7. The CT specimens were fatigue precracked in the test environment at temperature and load ratio R = 0.3, frequency of ≈1 Hz, and maximum stress intensity factor K_{max} of 20–25 MPa·$m^{1/2}$. After ≈0.5–mm crack extension, R was increased incrementally to 0.7, and the loading waveform changed to a slow/fast sawtooth with rise times of 30–1000 s. The SCC growth rates were determined using a trapezoidal waveform with R = 0.5 or 0.7, 12–1000 s rise time, 3600–s hold period at peak, and 12 -s unload time. This loading sequence is considered to result in reproducible CGRs.[105] During individual test periods, K_{max} was maintained approximately constant by periodic load shedding (less than 2% decrease in load at any given time).

Crack extensions were monitored by the reversing DC potential difference method. The current leads were attached to the holes on the top and bottom surfaces of the specimen (Fig. 60) and the potential leads were welded on the front face of the specimen across the machined notch but on diagonal ends. Also, to compensate for the effects of changes in resistivity of the material with time, an Alloy 600

internal reference bar was installed near the test specimen. The CT specimen and reference bar were connected in series, and the DC potential across the specimen as well as the reference bar was monitored continuously during the test. The results for the reference bar were used to normalize potential drop measurements for the CT test specimen. The stress intensity factor range ΔK was calculated as follows:

$$\Delta K = \frac{\Delta P}{\left(B B_N W\right)^{1/2}} \frac{\left(2+\frac{a}{W}\right)}{\left(1-\frac{a}{W}\right)^{3/2}} f\left(\frac{a}{W}\right), \tag{15}$$

$$\Delta P = P_{max} - P_{min} \qquad \text{for } R > 0, \tag{16}$$

$$f\left(\frac{a}{W}\right) = 0.886 + 4.64\left(\frac{a}{W}\right) - 13.32\left(\frac{a}{W}\right)^2 + 14.72\left(\frac{a}{W}\right)^3 - 5.6\left(\frac{a}{W}\right)^4, \tag{17}$$

where P_{max} and P_{min} are maximum and minimum applied load, a is crack length, W is the specimen width, and the effective thickness $B_{eff} = (B\ B_N)^{0.5}$. The applied K for the tests was in accordance with the specimen size criteria of ASTM E–1681 and E–647. These criteria are intended to ensure applicability and transferability of the cracking behavior of a component or specimen of a given thickness under a specific loading condition to a crack associated with a different geometry, thickness, and loading condition. The K/size criteria require that the plastic zone at the tip of a crack is small relative to the specimen geometry. For constant load tests, ASTM E–1681 requires that

$$B_{eff} \text{ and } (W-a) \geq 2.5\ (K/\sigma_{ys})^2, \tag{18}$$

and for cyclic loading ASTM–647 requires that

$$(W-a) \geq (4/\pi)\ (K/\sigma_{ys})^2, \tag{19}$$

where K is the applied stress intensity factor, and σ_{ys} is the yield stress of the material. For high–strain hardening materials, i.e., materials with an ultimate-to-yield stress ratio $(\sigma_{ult}/\sigma_{ys}) \geq 1.3$, both criteria allow the use of the flow stress defined as $\sigma_f = (\sigma_{ult} + \sigma_{ys})/2$ rather than the yield stress.

After the test the specimen was fractured in liquid nitrogen, and the fracture surfaces were examined by optical or electron microscopy to measure the final crack length using the 9/8 averaging technique; the two near–surface measurements were averaged, and the resultant value was averaged with the remaining seven measurements. The number of measurements was increased for irregular crack fronts.

5.2.4 Material Characterization

5.2.4.1 Alloy 600 for the Round Robin Specimen

This section presents the results of the metallographical characterization conducted on the alloy used in the round robin test. The alloy coupons used were cut to examine the microstructure on both the

plane of the crack and the plane normal to the plane of the crack. These coupons were first mechanically polished with 1–μm diamond paste, then electrochemically etched in either a 5% nital solution at 5 V to show grain boundaries, or a 70% phosphoric acid solution at 5 V to show the carbides.

Figure 63 shows the microstructure on the plane normal to that of the crack. The micrographs were taken from the same area, after the nital etch (Figs 63a, b) and after the phosphoric acid etch (Figs. 63c,d). Both etchants revealed a mictostructure with a grain size of approximately 35 μm, with a good intergranular and matrix carbide coverage. Titanium-rich precipitates were also observed, e.g. those shown in the upper center of Figs. 63c, d.

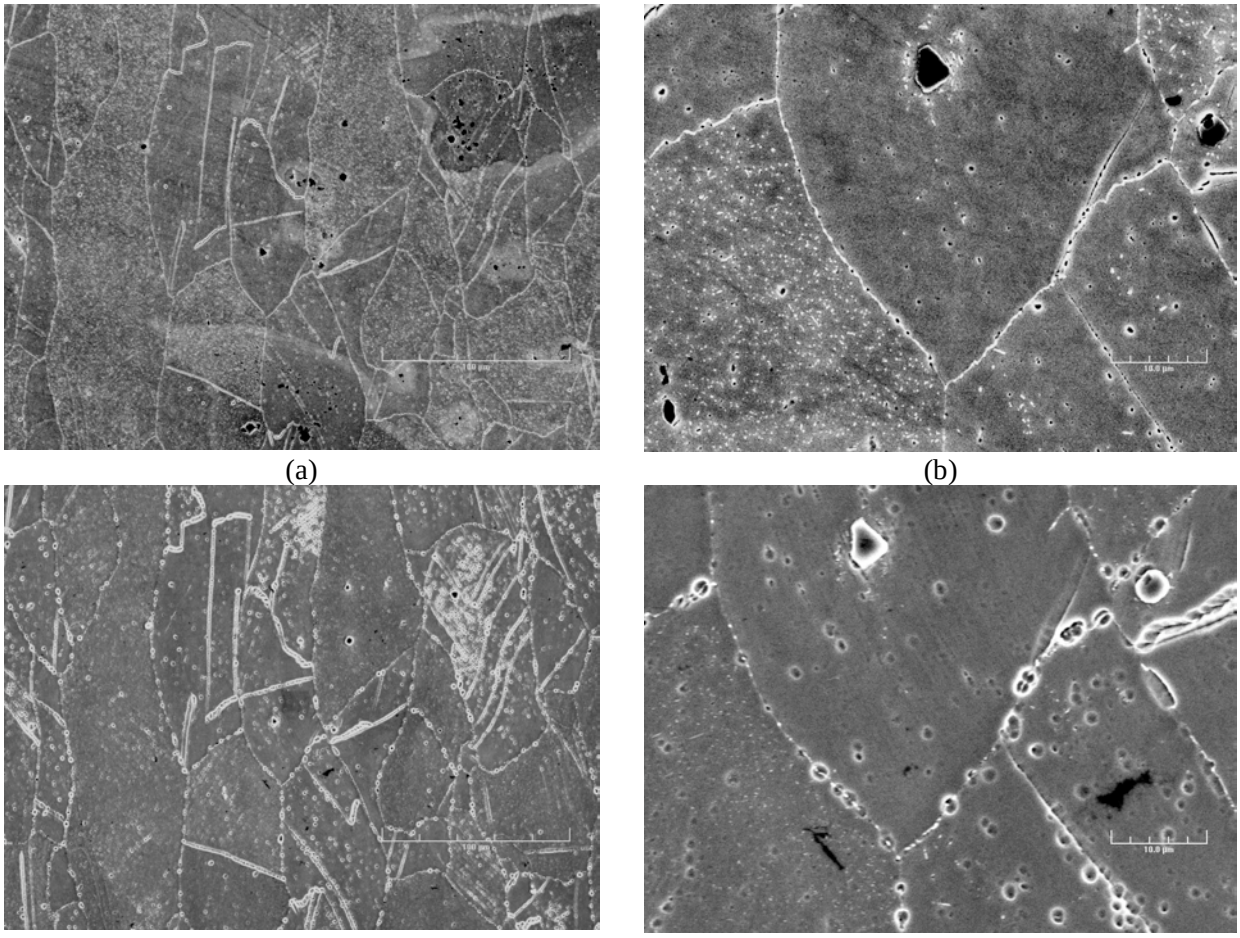

(a) (b)

(c) (d)

Figure 63. Microstructure of the round robin Alloy 600 etched with (a, b) nital and (c, d) phosphoric acid solution.

Figure 64 shows two magnifications of the microstructure on the plane parallel to that of the crack following a phosphoric acid etch. We observe that the etchant attacked different grains in different manners, suggesting the presence of matrix precipitates in some grains and the absence of precipitates in others.

In support of the previous observation, Figs. 65a,b show the microstructure of the round robin alloy, and Figs. 65c,d show the microstructure of a similar Alloy 600 used previously in our laboratory (CT31-01). Unlike the round robin alloy, the laboratory heat has an uniform distribution of carbides both

on the grain boundaries and in the matrix, with carbides on the grain boundaries being, as expected, larger in size than those in the matrix.

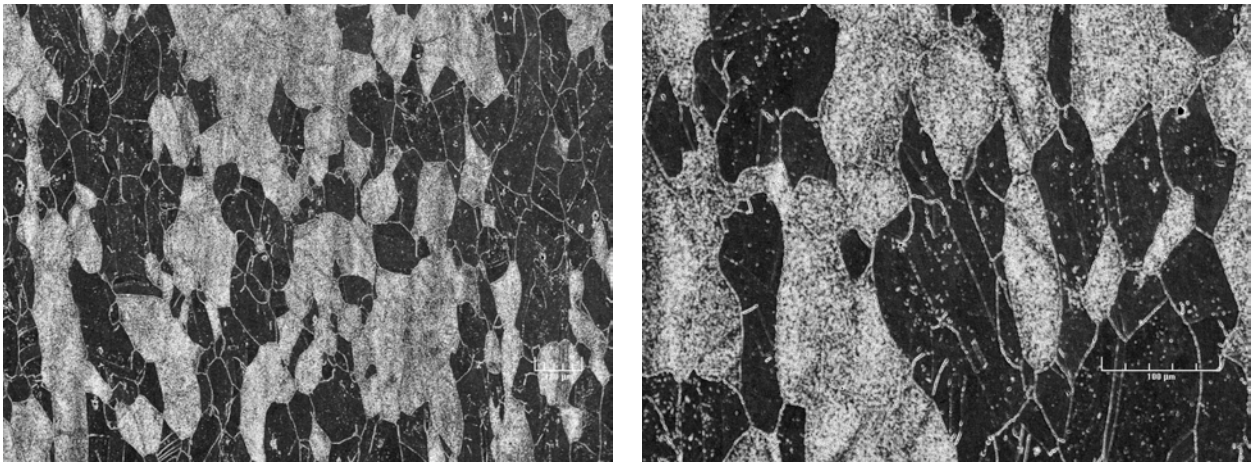

(a) (b)

Figure 64. Microstructure of the round robin alloy in the plane of the crack at two magnifications.

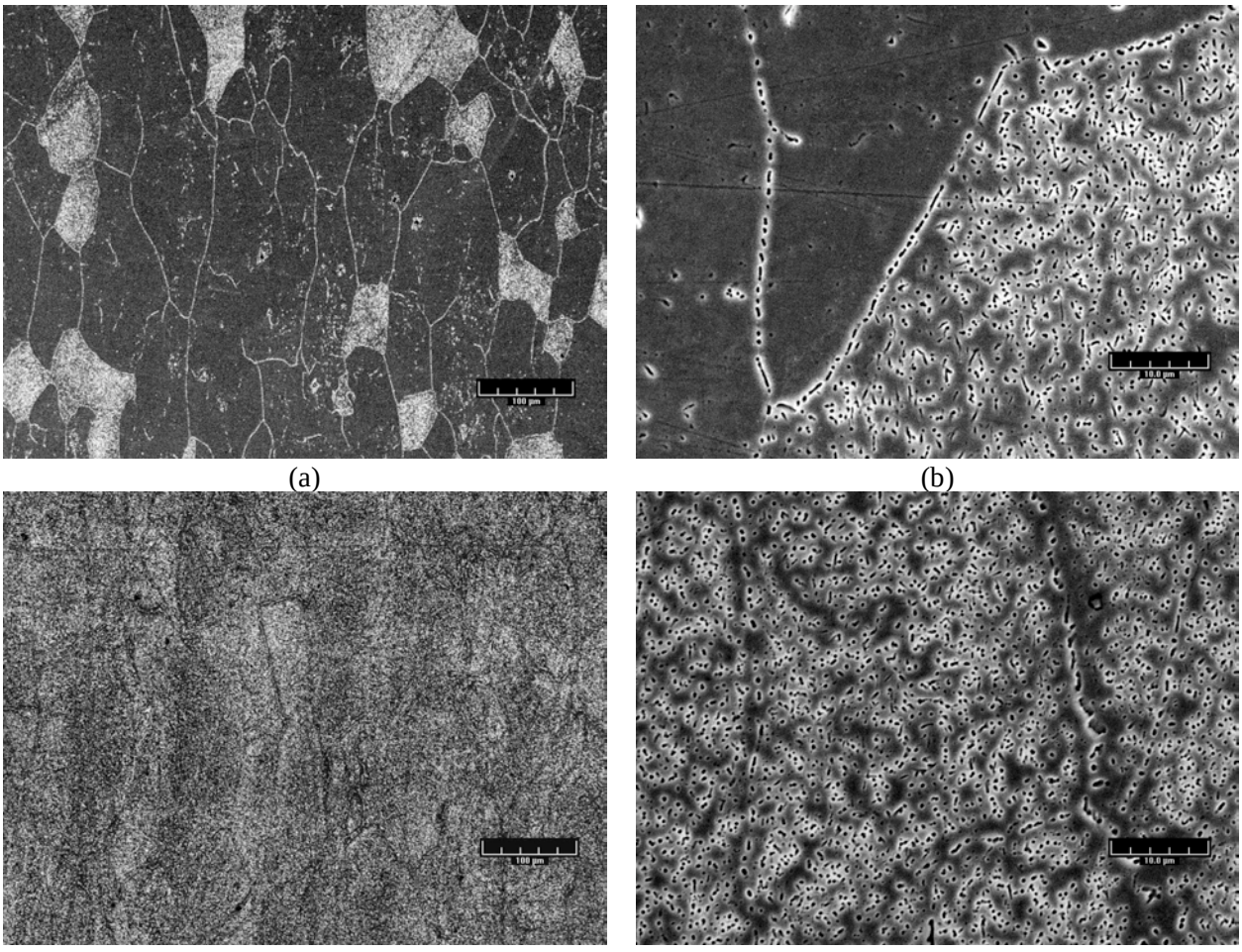

(a) (b)

(c) (d)

Figure 65. Microstructure of the round robin alloy in the plane of the crack at two magnifications (a,b) and that of a different heat of Alloy 600, used previously in our experiments (c, d).

5.2.4.2 Double–J Weld

The microstructures of Ni–alloy weld metals such as Alloy 182 and 82 are similar to those of wrought Alloys 600 and 690. Under certain thermal treatments, Cr–rich carbides can precipitate at both interdendrite and intradendrite grain boundaries.[106] Chromium depletion also occurs at the boundaries that are covered with such carbides. The precipitate phases are predominantly $M_{23}C_6$ and Ti–rich MC carbide. During the welding process, only the $M_{23}C_6$ carbide precipitates because of the rapid cooling of the weld metal from fusion temperature. Nucleation of M_7C_3 carbides requires long periods at relatively high temperatures, whereas nucleation of $M_{23}C_6$ is quite rapid and cannot be avoided even during water quenching from solution treatment temperatures. The matrix also contains a uniform dispersion of spherical γ' phase (Ni_3Ti).

The greater susceptibility of Alloy 182 to SCC than Alloy 82 has been attributed to differences in Cr depletion observed in the two alloys because of differences in their composition. Alloy 182 contains higher concentrations of C and Fe and a lower concentration of Cr, all of which enhance Cr depletion during carbide precipitation.

Weld Microstructure

A metallographic examination was performed to characterize the microstructure of the weld. For this purpose, three 1 cm × 2 cm rectangular pieces, designated 1, 2, and 3, were cut from the Alloy 182 weld (Fig. 66). The thickness of all three samples was 0.5 cm. Sample 3 was further cut in half to enable the examination of both surfaces A and B, normal to the plane of Fig. 66.

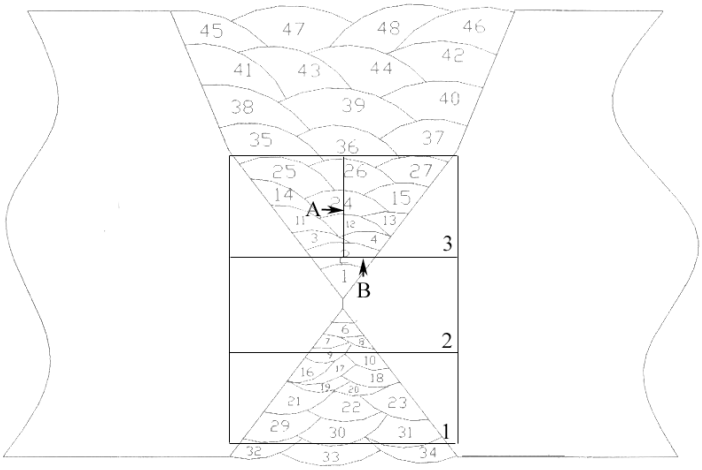

Figure 66. Schematic showing the locations of the three samples cut from the weld.

All samples were mechanically polished through 1–μm diamond paste, followed by electrolytic etching in a 70% H_3PO_4 and water solution at 5 V. The samples were then examined in a JEOL JSM-6400 SEM. Figure 67a shows the entire span of the weld microstructure on Sample 1 (the picture shown here was rotated by 90° with respect to the schematic shown in Fig. 66 to fit on the page). The elongated grains with dendritic features are easily discernible from the regular microstructure of Alloy 600 (upper-left and bottom-left corners). This difference is also visible in Fig. 67b. Figures 67c and 67d also show the dendritic microstructure in the weld. Large variations in grain size were evident between the different passes.

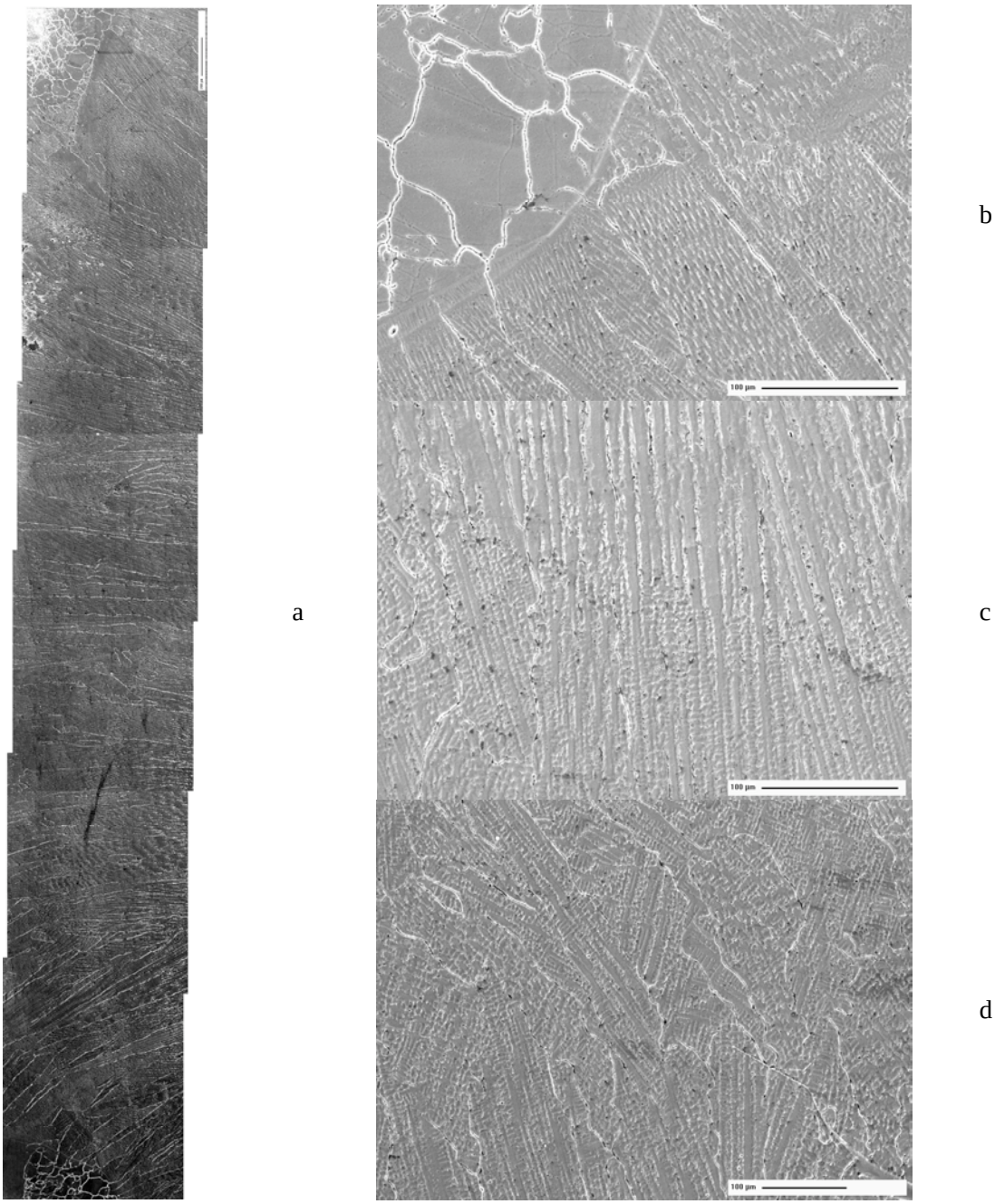

Figure 67. (a) Weld microstructure from Sample 1 (rotated 90° with respect to Fig. 9); (b) transition area between the weld and Alloy 600; and (c,d) dendritic microstructure in the weld.

Figure 68 focuses on the transition area between the weld and the base material, i.e., the HAZ. A larger grain size than that of the base material is observed in the immediate vicinity of the well in both Figs. 68a and 68b. These micrographs were obtained from two different, opposite locations on Sample 1. A dendritic microstructure was observed on the 3A plane (Fig. 66), and examples are shown in Fig. 69. The picture shown in Fig. 69a was taken at a location where the grain is still visible; however, internal dendritic features are apparent. Figure 69b was obtained at a weld pass, showing the different structures of the two weld layers.

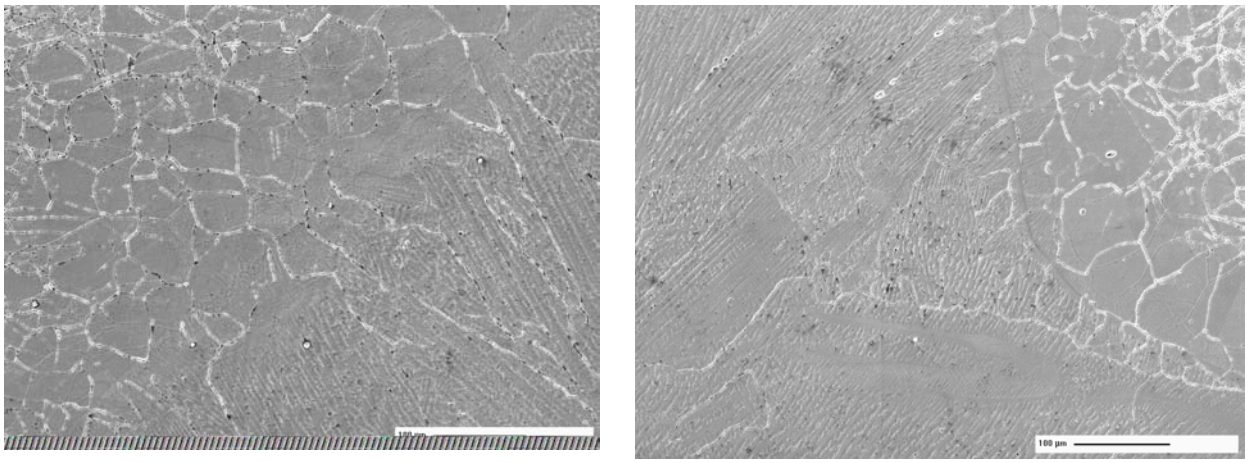

(a) (b)

Figure 68. Large grain microstructure in the HAZ at two opposite positions (a and b).

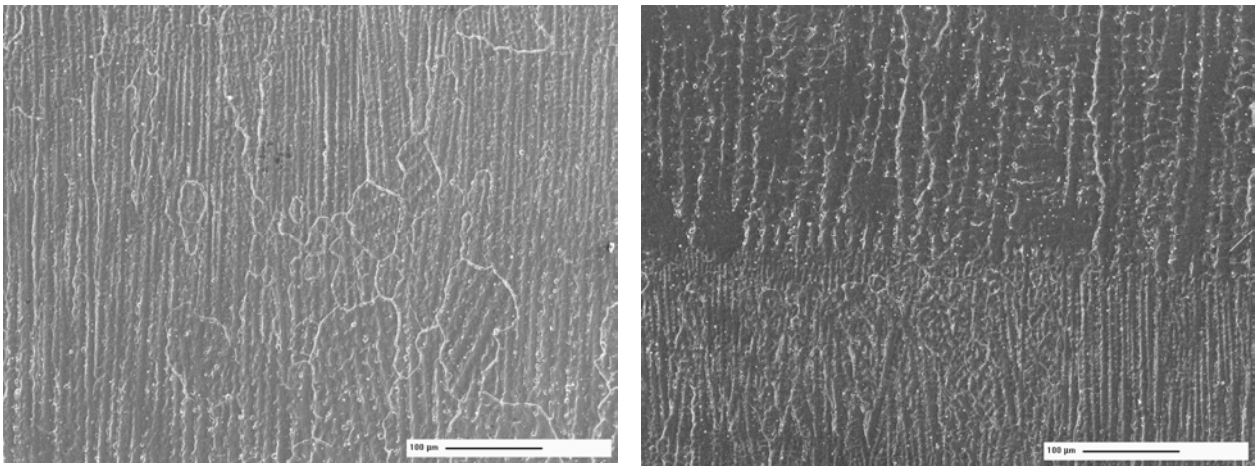

(a) (b)

Figure 69. (a) Dendritic microstructure on sample 3A, and (b) at a weld pass.

Figures 70a and b are micrographs obtained on the 3B plane at weld passes. Figure 70c and d are higher magnification micrographs obtained at locations in Figs. 70a and b, respectively. The grain as well as the dendritic microstructure are visible; however, as expected, the grains are more regular and the dendrites are perpendicular to the plane of observation.

Figure 71a is another example of microstructure obtained on the 3B plane at a weld pass. Fig. 71b is a higher magnification micrograph obtained at a location in Fig. 71a. From the manner in which the phosphoric acid attacked the grain boundaries, it appears that grain boundary precipitates were present. Additional precipitates or particles are also observed in both grain boundaries and matrix which have not been attacked by the phosphoric–acid etch.

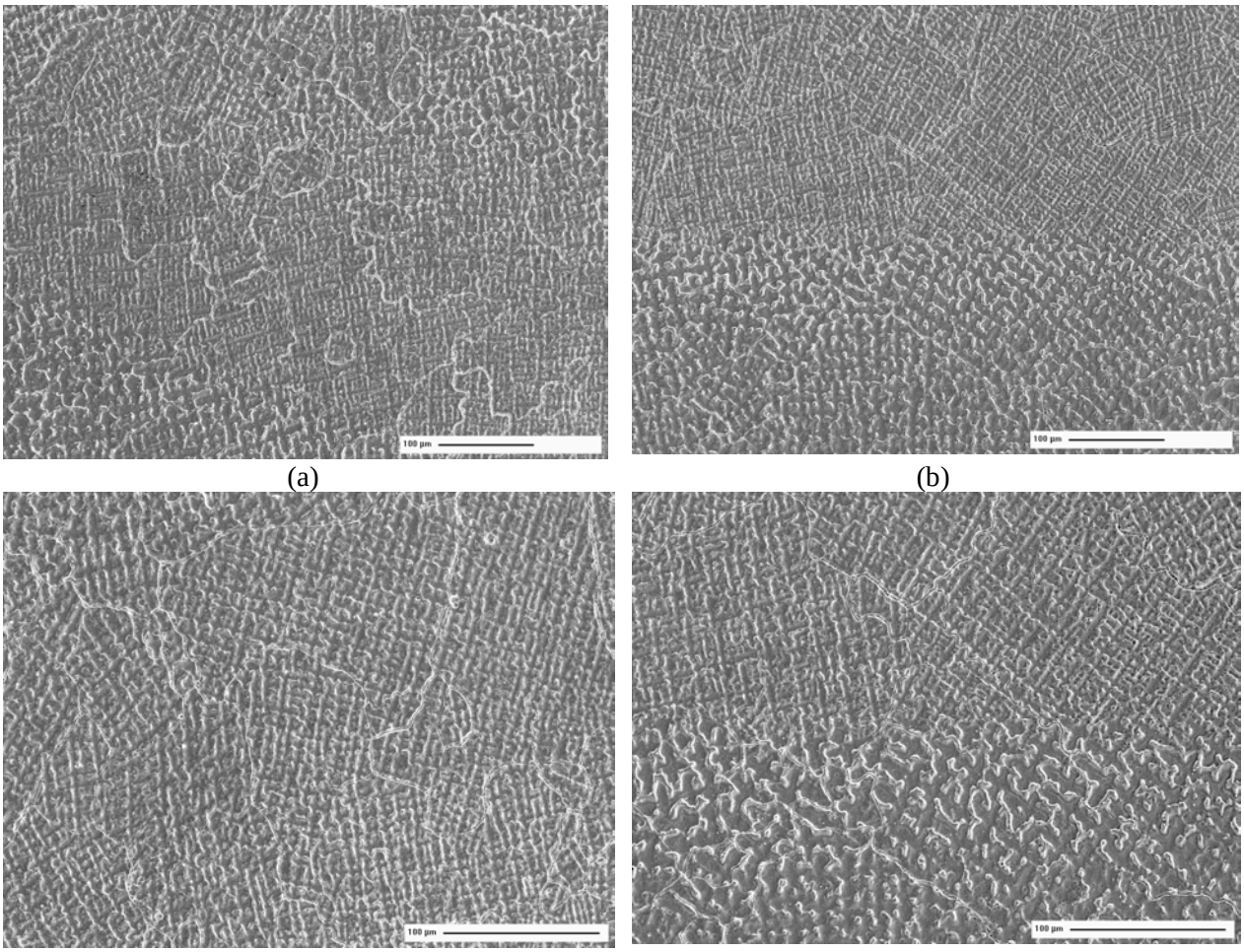

(a) (b)

(c) (d)

Figure 70. Examples of dendritic microstructure at a weld passes on sample 3B (a,b) and high magnification micrographs at the respective locations (c,d).

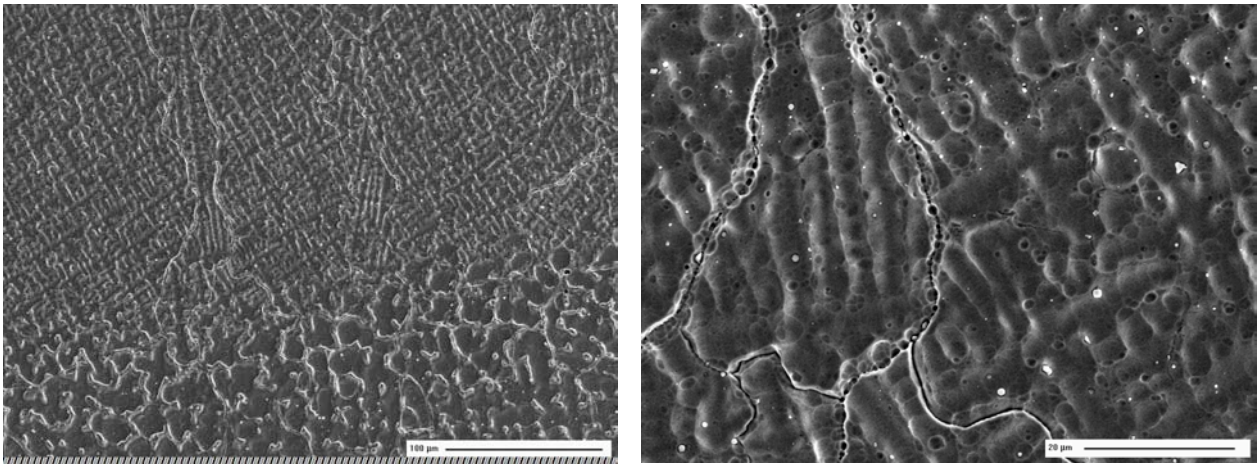

(a) (b)

Figure 71. (a) Dendritic mictostructure on sample 3B and (b) high magnification of a region from (a).

Examination of weld by SEM/EDX

Scanning electron microscopy and energy dispersive x–ray (SEM/EDX) analysis was conducted on sample 3A in a Philips XL30 FEG SEM. This sample was mechanically polished with 1–μm diamond paste, followed by electrolytic etching in a 70% H_3PO_4 and water solution at 5 V. Figure 72a,b shows the microstructure observed on the surface of sample 3A, at several magnifications. The elongated grains with dendritic features observed previously can be seen in all micrographs.

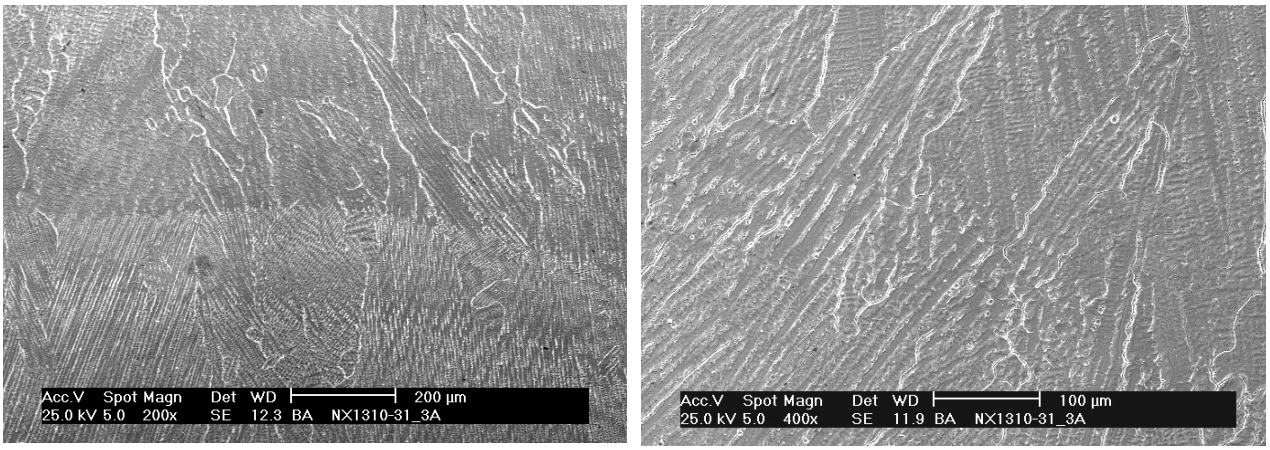

(a) (b)

Figure 72. Dendritic microstructure observed on the surface of sample 3A at (a) 100× and (b) 200× magnifications.

The objective of this part of the analysis was to investigate the nature of both matrix and grain boundary precipitates. Figure 73a shows one of the matrix precipitates on the surface of sample 3A. In Fig. 73b the EDX spectra resulting from the bulk and the precipitate are shown. Comparison of the two spectra allows for the observation that both the Ti and O peaks are higher in the spectrum resulting from the precipitate, suggesting that the particle is TiO_2. The compositional results of the analysis are shown in Table 13, confirming that indeed the precipitates are TiO_2.

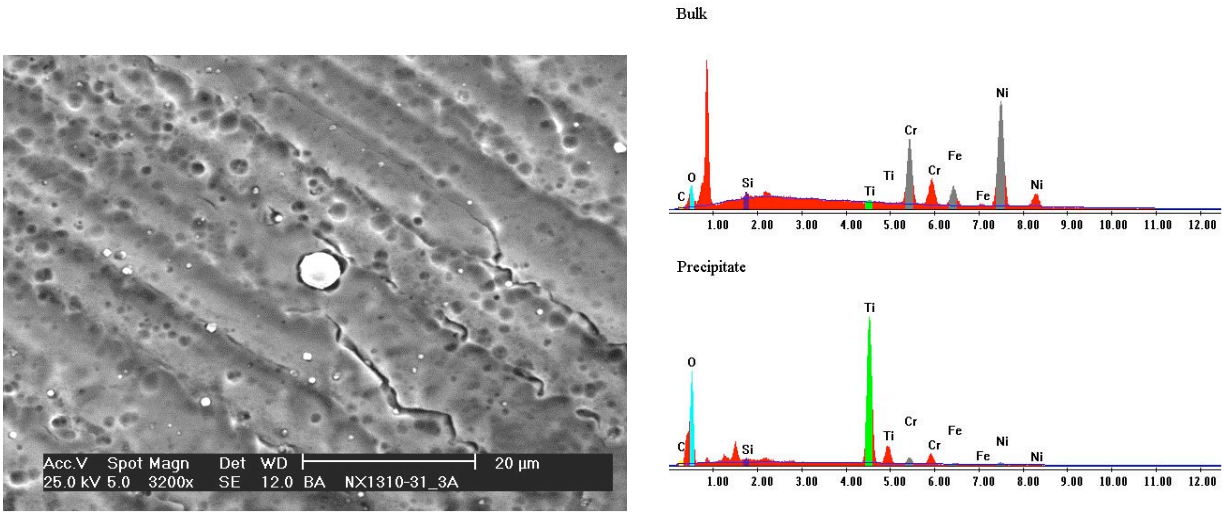

(a) (b)

Figure 73. (a) Micrograph showing one of the matrix precipitates observed on the surface of sample 3A and (b) EDX spectra resulting from the bulk and the precipitate shown in (a).

Table 13. Chemical compositions of the bulk material and matrix precipitate resulting from EDX analysis.

	Bulk		Matrix precipitate	
	wt. %	at. %	wt. %	at. %
C	1.53	6.56	1.66	3.63
O	**1.77**	**5.72**	**39.08**	**64.24**
Si	0.60	1.10	0.56	0.52
Ti	**0.48**	**0.52**	**50.15**	**27.54**
Cr	15.20	15.08	3.83	1.94
Fe	7.30	6.74	1.06	0.50
Ni	73.12	64.27	3.67	1.64
Total	100.00	100.00	100.00	100.00

Next, the nature of the grain boundary precipitates was investigated. Figure 74a shows the microstructure on plane "A" (Fig. 66), while Fig. 74b is a higher magnification micrograph showing both matrix and grain boundary precipitates. In Fig. 74c EDX spectra resulting from the bulk and from the grain boundary precipitate are shown. The comparison of the two spectra as well as the quantitative results shown in Table 14 suggest that the grain boundary precipitate is TiO_2.

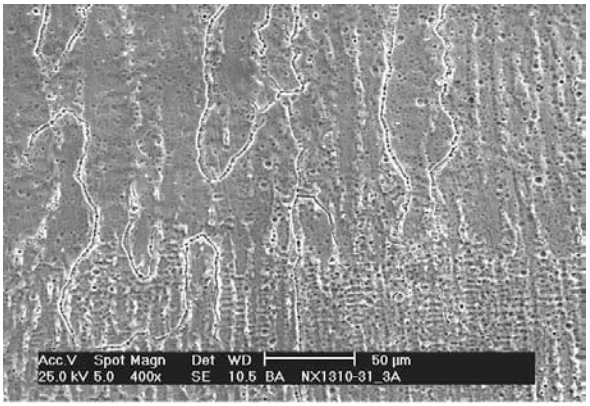

(a)

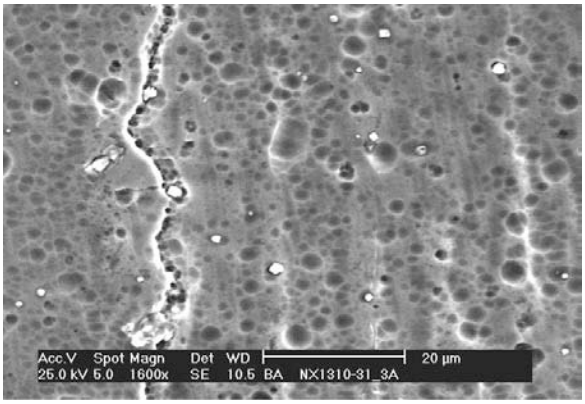

(b)

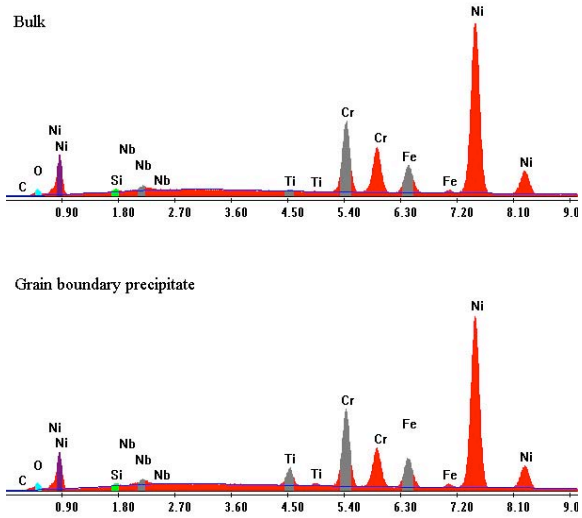

(c)

Figure 74.
Micrographs showing (a) the microstructure on plane 3A, and (b) matrix and grain boundary precipitates, and (c) EDX spectra resulting from the bulk and from the grain boundary precipitate shown in (b).

Table 14. Chemical compositions of the bulk material and grain boundary precipitate resulting from EDX analysis.

	Bulk		GB precipitate	
	wt. %	at. %	wt. %	at. %
C	1.34	5.82	1.65	6.99
O	**1.94**	**6.33**	**2.25**	**7.18**
Si	0.75	1.39	0.62	1.13
Nb	2.14	1.20	2.26	1.24
Ti	**0.30**	**0.32**	**2.70**	**2.87**
Cr	14.23	14.26	14.73	14.44
Fe	7.27	6.78	7.41	6.76
Ni	72.03	63.90	68.38	59.38
Total	100.00	100.00	100.00	100.00

The microstructure on plane "A" (Fig. 66) was further examined in the Hitachi S-4700 field emission gun SEM, allowing a close inspection of the precipitates and grain boundary continuity across the HAZ. Figures 75a, c are high magnification micrographs showing Ti–rich precipitates in the weld material, in both matrix and grain boundaries. Figures 75b, d are maps showing the topography at the locations where the high magnification micrographs were taken.

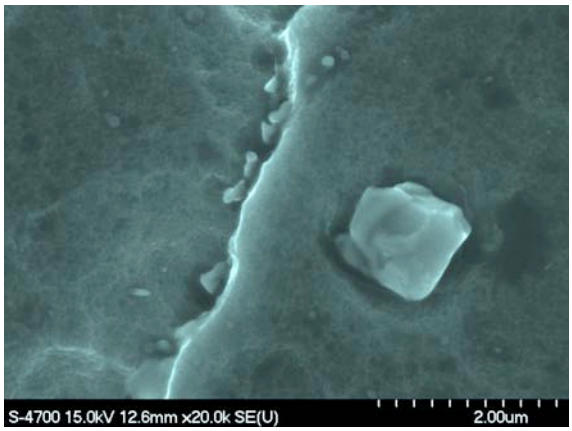

(a)

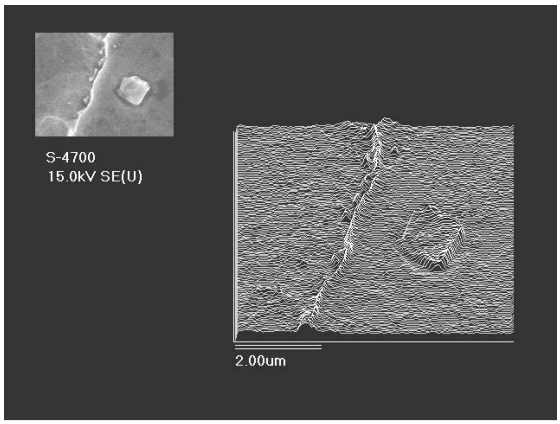

(b)

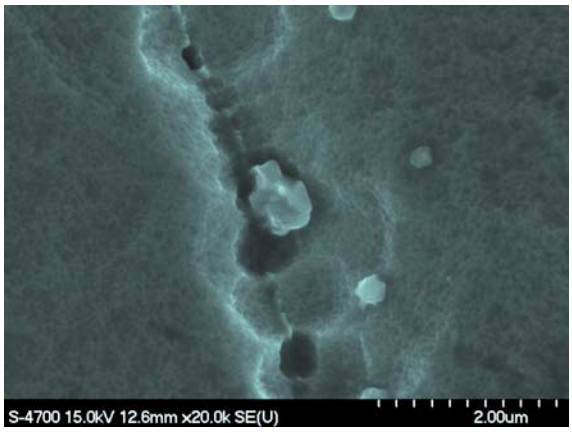

(c)

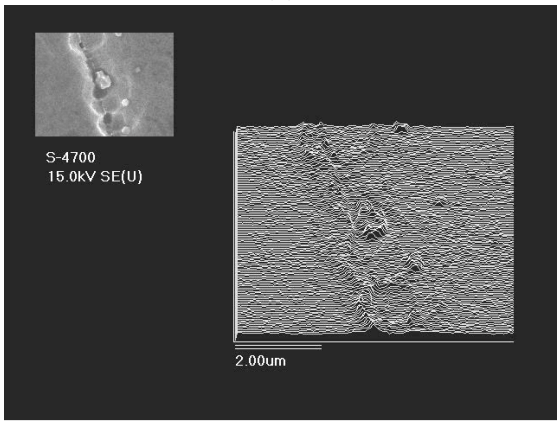

(d)

Figure 75. Micrographs showing Ti-rich precipitates in the weld material (a,c), and maps showing the topography at the locations where the high magnification micrographs were taken (b,d).

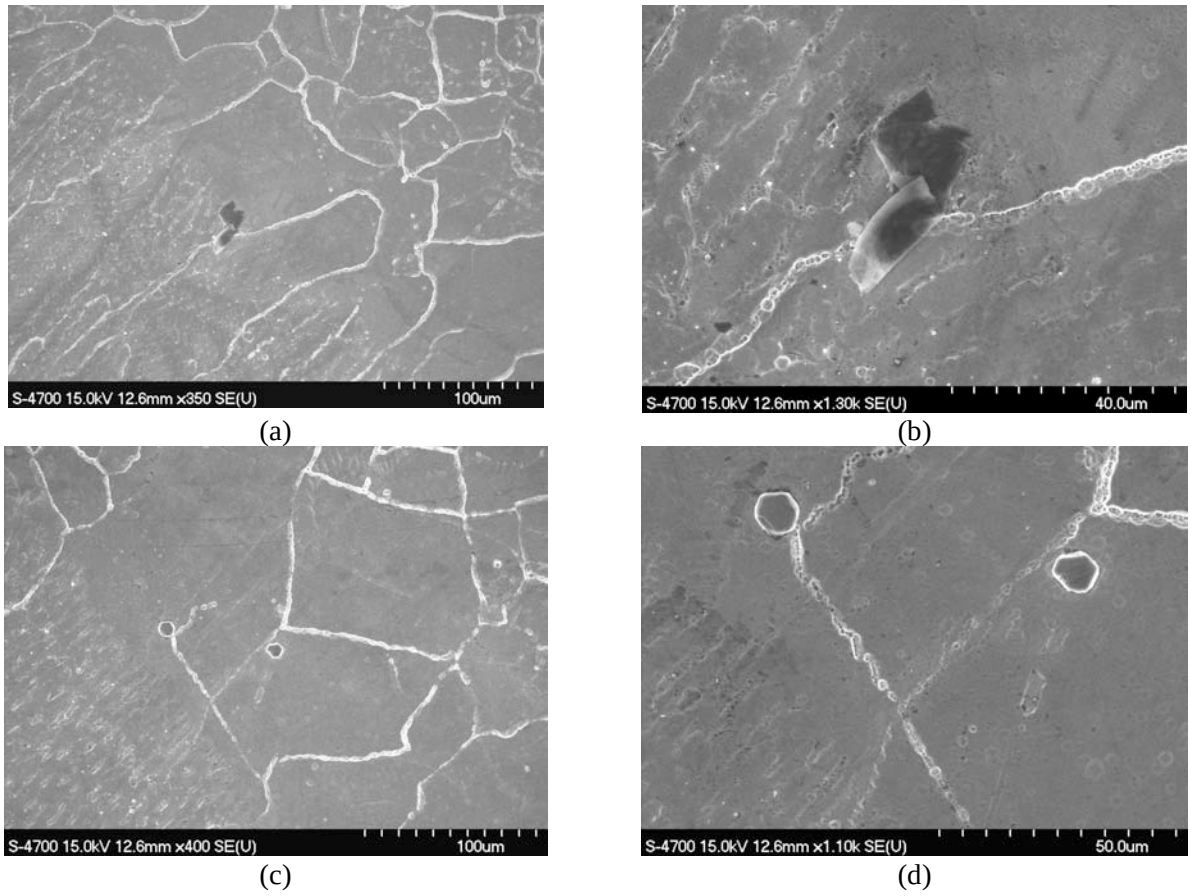

Figure 76. Micrographs showing the heat affected zone (a,c), and high magnification micrographs showing precipitates in the heat affected zone (b,d).

Figures 76a, c show areas on the HAZ where the dendritic microstructure (lower left) is replaced by the large grains of the HAZ. Figures 76b, d are high magnification micrographs of the precipitates observed in Figs. 76a, c, respectively. Figure 76 also shows that the random, high–angle boundaries from the weld extend into the HAZ.

In summary, the metallographic examination of the weld alloy has found that there exists a large variation in grain size between the different weld passes. Both matrix and grain boundary precipitates were observed, and these were identified to be TiO_2. The effect of TiO_2 precipitates on the SCC behavior is unknown. High angle boundaries were observed to extend from the weld into the HAZ, and the implication of this observation is that once a crack initiates in the HAZ, it can then readily extend into the weld via such continuous, cracking-susceptible boundaries.

Examination of Weld specimens by Orientation Imaging Microscopy

Orientation imaging microscopy (OIM) is a diffraction-based technique by which maps of the crystal structure of a material can be obtained, thereby providing both the orientations of the crystals (grains) and the types of grain boundaries present. The interest to apply the OIM technique to the current weld samples was driven by two features (that OIM can analyze) that have been shown to influence strongly the intergranular stress corrosion cracking behavior of austenitic alloys in high temperature aqueous environments: the grain boundary character distribution (i.e., the proportions of boundaries in special orientation relationships), and the amount and location of residual stress.

For the preliminary OIM analysis reported here, specimen 3B was first mechanically polished with 1–μm diamond paste on both surface and plane "B" (see Fig. 66), and electro-polished in a perchloric acid (10%) and methanol solution at –50°C. Repeated double polishing cycles of 5 s at 40 V provided the best surface finish.

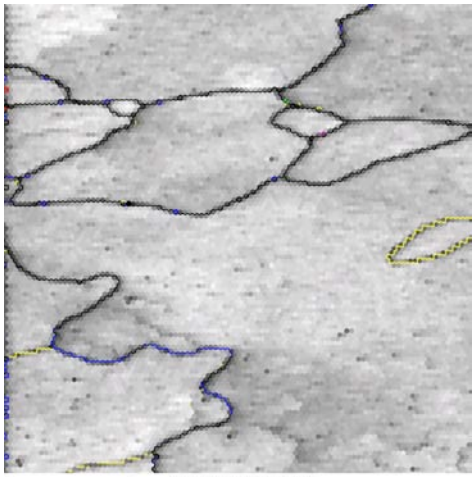

(a)

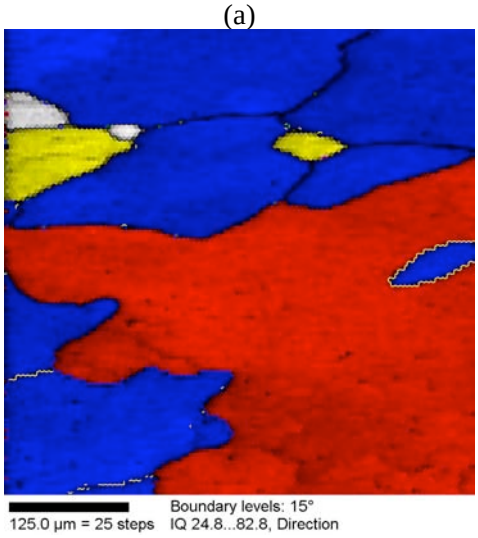

(b)

Gray Scale Map Type: Image Quality
24.8...82.8 (24.8...82.8)

Color Coded Map Type: Crystal Direction

Direction	Min	Max	Total Fraction	Partition Fraction
<1 0 0>||[0 0 1]	0°	15°	0.465	0.465
<0 1 1>||[0 0 1]	0°	15°	0.036	0.036
<1 1 1>||[0 0 1]	0°	15°	0.000	0.000
<1 1 2>||[0 0 1]	0°	15°	0.000	0.000
<1 1 4>||[0 0 1]	0°	15°	0.488	0.488

Boundaries: Rotation Angle

Min	Max	Fraction
15°	180°	0.883

Boundaries: CSL

Sigma	Tolerance	Fraction	Volume	MDF Value
1	15.00	0.117	0.0228	5.14
3	8.66	0.005	0.0176	0.26
5	6.71	0.006	0.0123	0.50
7	5.67	0.000	0.0099	0.00
11	4.52	0.005	0.0075	0.72
13a	4.16	0.001	0.0029	0.26
13b	4.16	0.012	0.0039	2.96
15	3.87	0.097	0.0094	10.29
17a	3.64	0.006	0.0020	3.15
17b	3.64	0.006	0.0039	1.58
19a	3.44	0.005	0.0033	1.63
19b	3.44	0.000	0.0022	0.00
21a	3.27	0.000	0.0019	0.00
21b	3.27	0.000	0.0057	0.00
23	3.13	0.000	0.0050	0.00
25a	3.00	0.000	0.0011	0.00
25b	3.00	0.000	0.0044	0.00
9	5.00	0.002	0.0102	0.15
27a	2.89	0.002	0.0020	1.18
27b	2.89	0.000	0.0039	0.00
summary	-	0.264	0.1317	2.01

*For statistics - any point pair with misorientation exceeding 2° is considered a boundary

(c)

Figure 77. (a) OIM map of the weld, on plane "B", sample 3B; (b) the same OIM map showing the orientation of each grain; and (c) legends for crystal directions and the resulting grain boundary character distribution.

Figure 77a shows an OIM map resulting from the weld, plane B. In this analysis, the grain boundaries were classified according to the coincident site lattice model as low angle boundaries (LAB, $\Sigma=1$), coincident site lattice boundaries (CSLB, $3\leq\Sigma<29$), or high angle boundaries (HAB, $\Sigma\geq29$). Cracking would be expected along the high angle boundaries, identified as such, with black color in the OIM map. Also shown (Fig. 77b) is a map indicating the crystal directions parallel (±15°) to the normal sample surface. First, we observe that the dendritic structure does not appear in the OIM maps, suggesting that the dendrites are coherent, and, therefore, very unlikely to crack. Second, little or no texture (Fig. 77b) is evident on this plane ("B" in Fig. 66). Third, the proportion of crack-resistant coincident site lattice boundaries (CSLBs) is very low (26%), as indicated by the data in Fig. 77c. For

comparison, solution annealed Alloy 600 has a CSLB fraction of approximately 50%. If this last observation holds true for a larger area – where a statistically significant number of boundaries are analyzed – it in itself suggests a high degree of susceptibility of the weld.

Next, an area on the surface of sample 3B was mapped by OIM. The area included the weld, HAZ, and part of the Alloy 600, as shown in Fig. 78a. The resulting proportion of CSLBs was 35%. Although somewhat larger than in the previous example, this result was probably due to the inclusion of the area from Alloy 600 in the total count.

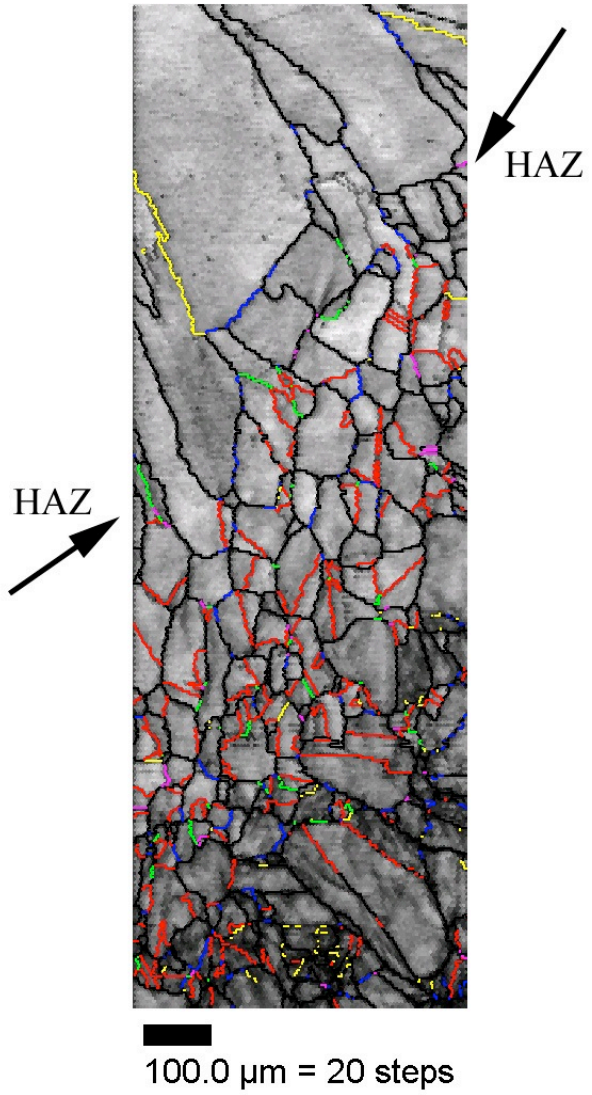

(a)

Gray Scale Map Type: Image Quality
16.9...77.5 (16.9...77.5)

Color Coded Map Type: <none>

Boundaries: Rotation Angle

Min	Max	Fraction
15°	180°	0.966

Boundaries: CSL

Sigma	Tolerance	Fraction	Volume	MDF Value
1	15.00	0.034	0.0228	1.48
3	8.66	0.226	0.0176	12.86
5	6.71	0.006	0.0123	0.45
7	5.67	0.010	0.0099	0.96
11	4.52	0.004	0.0075	0.47
13a	4.16	0.004	0.0029	1.39
13b	4.16	0.007	0.0039	1.70
15	3.87	0.001	0.0094	0.10
17a	3.64	0.001	0.0020	0.74
17b	3.64	0.006	0.0039	1.56
19a	3.44	0.006	0.0033	1.87
19b	3.44	0.001	0.0022	0.31
21a	3.27	0.001	0.0019	0.58
21b	3.27	0.002	0.0057	0.27
23	3.13	0.001	0.0050	0.15
25a	3.00	0.000	0.0011	0.15
25b	3.00	0.002	0.0044	0.52
9	5.00	0.026	0.0102	2.53
27a	2.89	0.005	0.0020	2.52
27b	2.89	0.007	0.0039	1.76
summary	-	0.348	0.1317	2.64

*For statistics - any point pair with misorientation exceeding 10° is considered a boundary

(b)

Figure 78. (a) OIM map on the surface of sample 3B and (b) the resulting grain boundary character distribution. The OIM map covers the weld (upper part), the HAZ (indicated by arrows), and Alloy 600 (lower part).

Figure 79a shows the same OIM map as Fig. 78a, but with the grain directions included. Again, no definitive conclusion can be drawn with respect to the presence or absence of a texture in the weld due to the small weld area analyzed. Nevertheless, we notice that, as in Fig. 77, the OIM did not distinguish the

dendritic structure (SEM micrograph of Fig. 79b was included for comparison). Thus, it is very likely that the grain boundary character distribution will determine the cracking behavior of the weld.

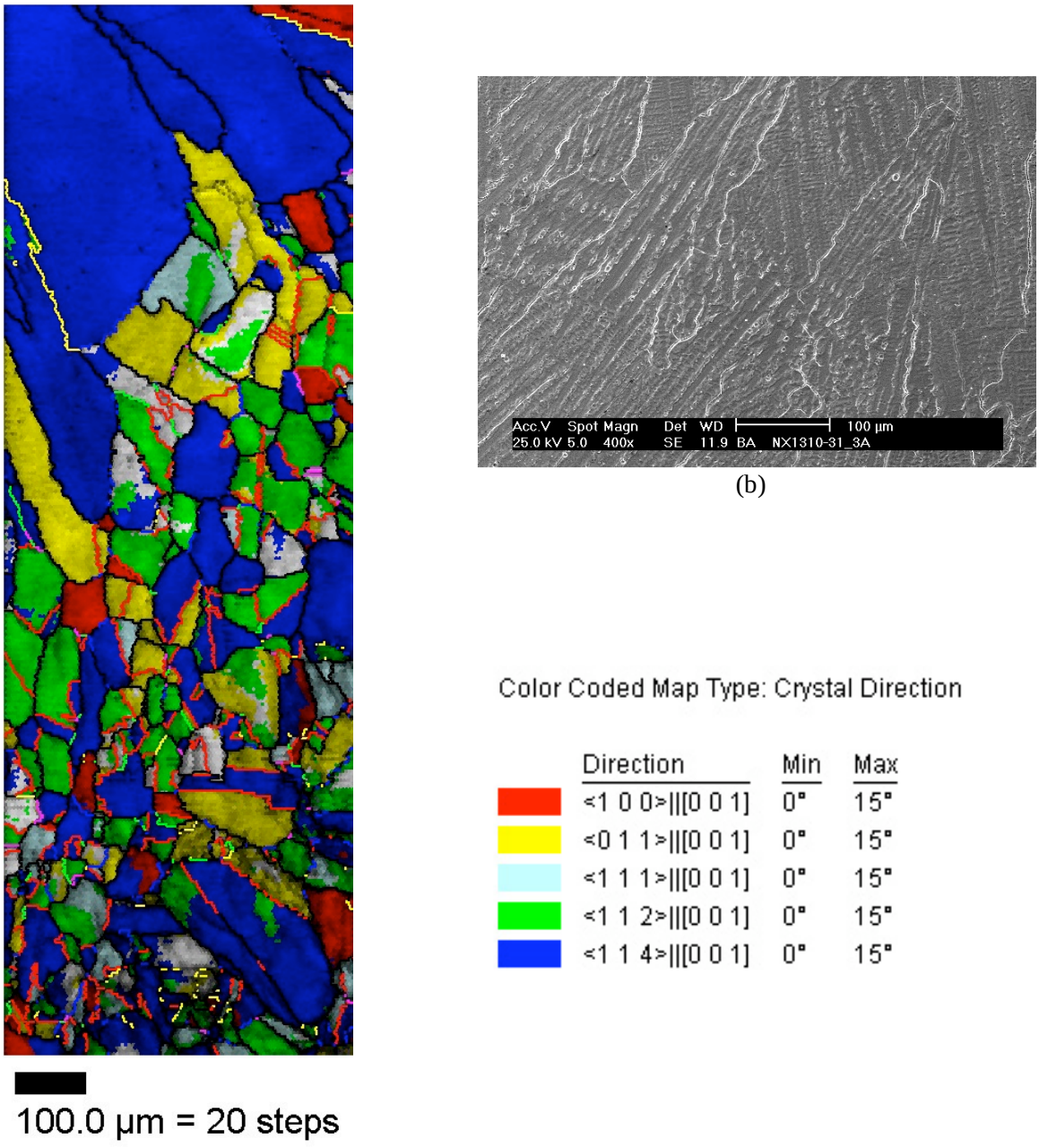

(b)

(a)

Figure 79. (a) The same OIM map as in Fig. 78a showing crystal directions and (b) SEM micrograph illustrating the dendritic microstructure of the weld.

In conclusion, the OIM analysis presented here has shown that the intragranular dendrites are coherent and are, therefore, expected to be resistant to cracking. In consequence, the grain boundary character distribution (along with residual deformation) that will likely determine the cracking behavior of the welds. The proportion of cracking-resistant CSL boundaries in the weld was found to be relatively small; however, a statistically significant population of boundaries needs to be analyzed to substantiate this last observation.

5.3 Results

5.3.1 Alloy 600 Round Robin Specimen

A CGR test was conducted on Alloy 600 round–robin specimen in simulated PWR environment at 320°C according to the testing protocol agreed upon by the participants of ICG–EAC. The round robin test protocol specifies a progression of loading conditions during the test, and are given in Table 15. The actual environmental and loading conditions and experimental CGRs for the test are given in Table 16; the changes in crack length and K_{max} with time during various test periods are shown in Fig. 80.

Table 15. Loading conditions for the Alloy 600 round-robin test.

Step	K_{max}, MPa $m^{1/2}$	Load Ratio, R	Frequency	Crack Increment
1	25	0.3	1 Hz sine	0.5 mm
2	28	0.5	1 Hz sine	0.3 mm
3	30	0.6	1 Hz sine	0.3 mm
4	30	0.7	1 Hz sine	0.3 mm
5	30	0.7	0.1 Hz sine	0.2 mm
6	30	0.7	0.01 Hz sine	0.2 mm
7	30	0.7	0.001 Hz triangle	0.2 mm
8	30	0.7	0.001 Hz + 9 ks hold	0.1 mm
9	30	Constant load	Constant load	≥1 month

Table 16. Crack growth results for Alloy 600[a] round robin specimen RR-1 in PWR water[b] at 320°C.

Test Period	Test Time, h	Conduc-tivity,[c] µS/cm	ECP A600/Pt, mV	R Load Ratio	Rise Time, s	Down Time, s	Hold Time, s	K_{max}, MPa·$m^{1/2}$	ΔK, MPa·$m^{1/2}$	CGR, m/s	CGR in Air, m/s	Crack Length, mm
1	146	25.7	-639/-660	0.3	0.5	0.5	0	24.8	17.4	2.01E-08	4.07E-08	20.619
1b	166	26.0		0.3	0.5	0.5	0	25.0	17.5	2.64E-08	4.23E-08	20.801
2	175	26.0		0.5	0.5	0.5	0	27.9	14.0	1.30E-08	2.85E-08	21.029
3	193	25.3		0.6	0.5	0.5	0	30.0	12.0	9.89E-09	2.13E-08	21.350
4	234	23.5		0.7	0.5	0.5	0	30.4	9.1	3.80E-09	1.02E-08	21.743
5	354	25.5	-670/-705	0.7	5	5	0	30.1	9.0	1.19E-09	9.83E-10	21.947
6	550	25.5		0.7	50	50	0	29.8	9.0	3.00E-10	9.44E-11	21.993
7a	642	26.3		0.7	500	500	0	29.6	8.9	2.55E-10	9.18E-12	22.124
7b	863	24.6	-666/-668	0.7	500	500	0	29.9	9.0	negligible	9.50E-12	22.108
3B	865	24.6		0.6	0.5	0.5	0	30.1	12.0	1.13E-07	2.16E-08	22.199
4B	871	27.4		0.7	0.5	0.5	0	30.1	9.0	1.45E-08	9.82E-09	22.385
5B	898	25.1		0.7	5	5	0	29.6	8.9	1.25E-09	9.19E-10	22.425
3C	904	25.1		0.6	0.5	0.5	0	30.0	12.0	1.90E-08	2.13E-08	22.501
4C	928	24.9		0.7	0.5	0.5	0	30.0	9.0	4.73E-09	9.63E-09	22.780
5C	1040	25.3		0.7	5	5	0	29.9	9.0	8.09E-10	9.55E-10	22.938
6C	1320	25.1	-658/-684	0.7	50	50	0	30.1	9.0	3.14E-10	9.72E-11	23.087
7C	1570	26.0		0.7	500	500	0	30.2	9.1	5.91E-10	9.86E-12	23.351

[a]Alloy 600 Heat 3110439 cold worked 30% (cross–rolled 15% per pass).
[b]Simulated PWR water with 2 ppm Li, 1100 ppm B, and 2 ppm dissolved hydrogen (≈23 cc/kg); O_2 concentration was always less than 10ppb.
[c]Represents values in the effluent; conductivity was ≈22.0 µS/cm in feedwater.

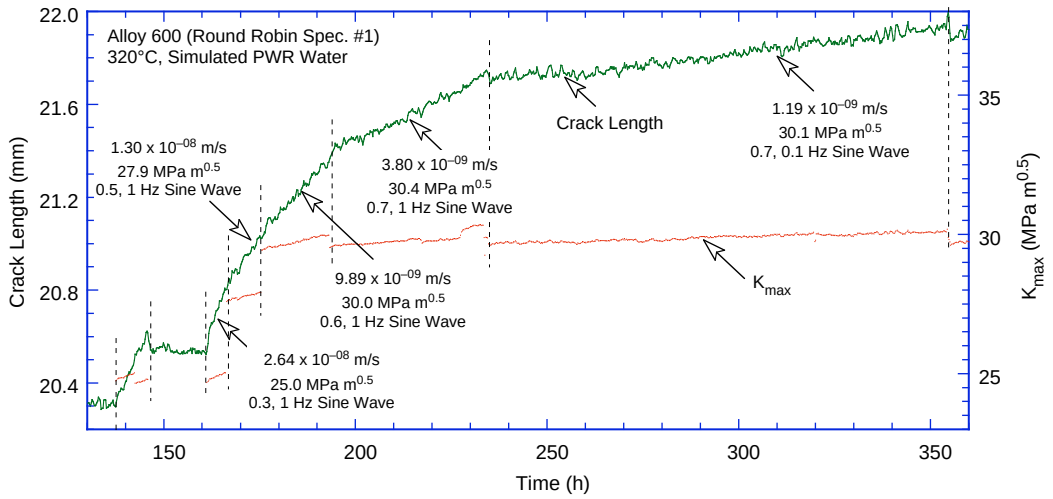

(a)

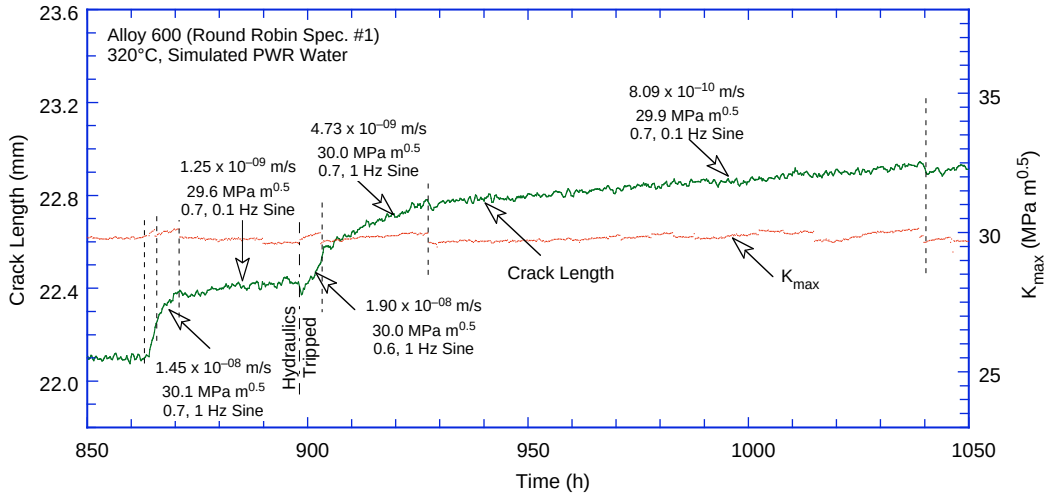

(b)

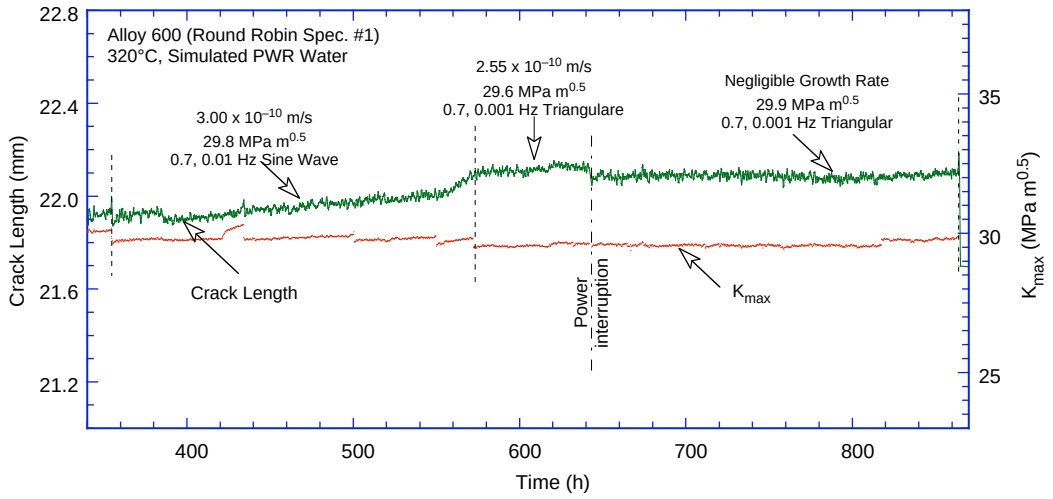

(c)

Figure 80. Crack length vs. time plot for Alloy 600 round-robin specimen RR-1 in simulated PWR environment at 320°C during periods (a) 1-5, (b) 3B-5C, (c) 6-7, and (d) 6C-7C.

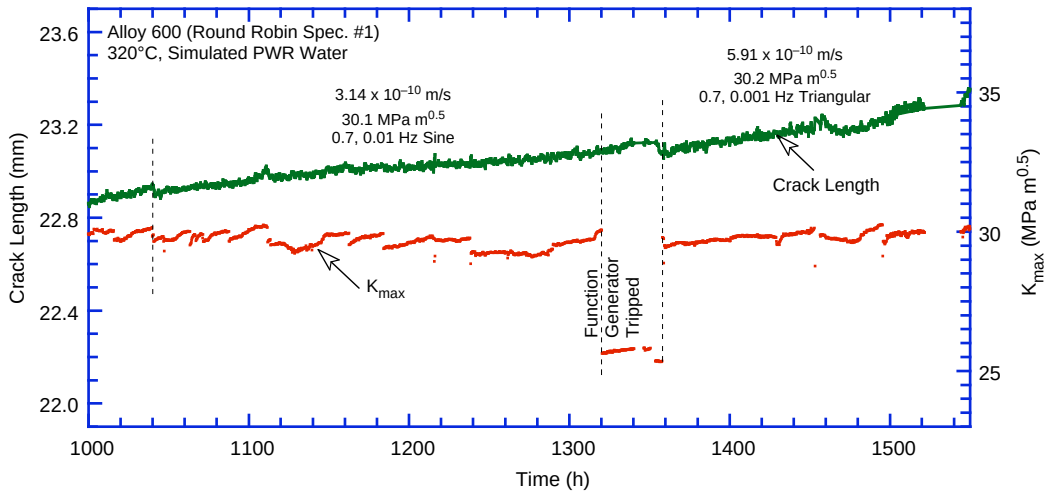

(d)

Figure 80. (Contd.)

The existing CGR data under cyclic loading indicate that in simulated PWR or low–DO water at 320°C only some heats of Alloy 600 show enhanced growth rates. For the heats that show environmental enhancement, the CGRs may be represented by the best–fit curve for Alloy 600 in high–purity water with 300 ppb DO at 289°C. The experimental CGRs from the present test and those predicted in air for the same loading conditions are plotted in Fig. 81. For high growth rates, the rates measured for the round robin specimen are a factor of ≈2 lower than those predicted in air. The difference, most likely, is due to the material condition; the round robin specimen was 30% cold worked, whereas the data in air are for annealed material. As expected, for low growth rates, the measured rates are higher than predicted in air.

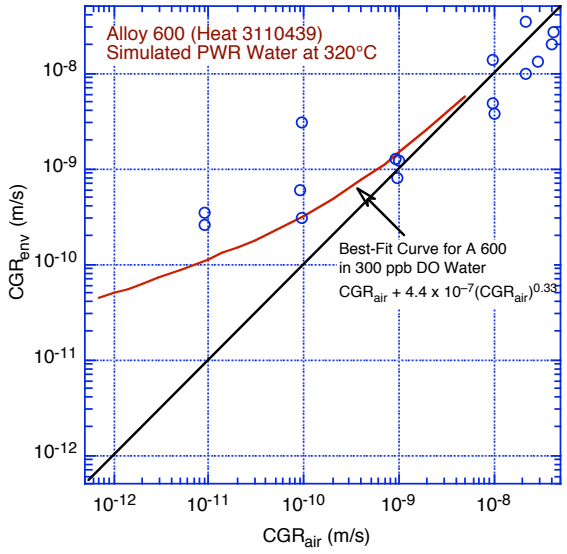

Figure 81.
CGR data for specimen RR-1 of the Alloy 600 round-robin test in simulated PWR environment at 320°C.

The test had to be stopped because of large pressure fluctuations and, finally, total flow blockage. The cause of flow blockage was identified to be $Al(OH)_3$ deposits. The source of Al in our system is the alumina insulators used for the DC potential and current leads. Because water is being recirculated without a purification system, the concentration of Al gradually builds up during operation, eventually leading to plugging of the cooler regions. The entire return line from the autoclave to the supply tank

including the back–pressure regulator was either replaced or cleaned by back flushing. For the remainder of the test, the water system was operated in a once–through mode to minimize the build–up of deposits.

The specimen was next fractured in preparation for metallographic examination. A photomicrograph of the broken half of the CT specimen is shown in Fig. 82. The crack front appears to be consistent with the observations in Switzerland; growth rates are significantly higher near the edge of the specimen than the center. For comparison, Fig. 83 shows the very similar fracture surface from round-robin specimen RR-3 reported by H. P. Seifert of Paul Sherrer Institute in Switzerland.* It is possible that since the round-robin specimens were fabricated from Heat 3110439 cold worked 30% (cross–rolled 15% per pass) the distribution of cold work may have not been uniform across the specimen thickness. The fracture mode is TG near the machine notch, followed by a transition region of highly angular, cleavage–like facets with "river" patterns, and changing to completely IG for most of the test. Also, finger–like regions of IG fracture extend ahead of the crack front near these secondary cracks.

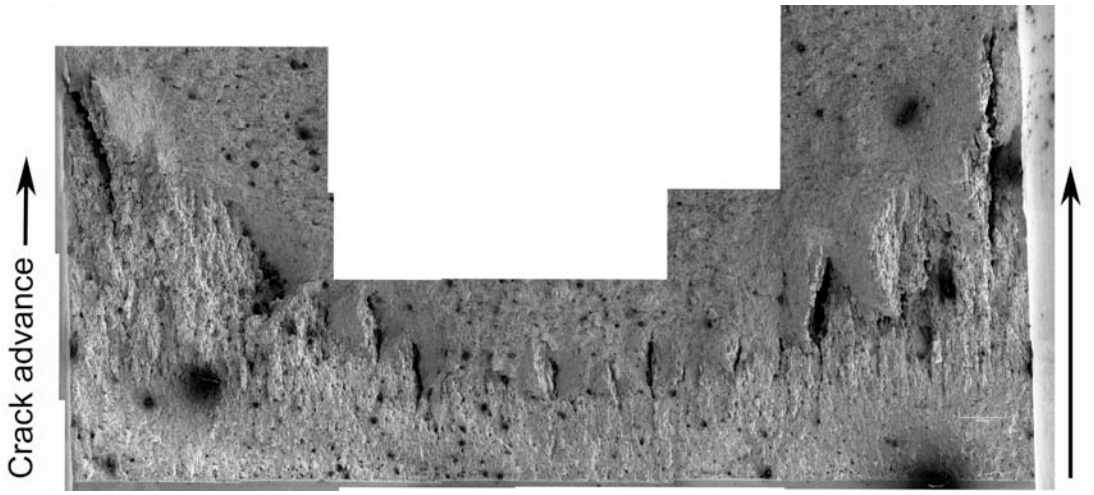

Figure 82. Entire crack surface of Alloy 600 round robin specimen RR-1 tested in PWR water at 320°C.

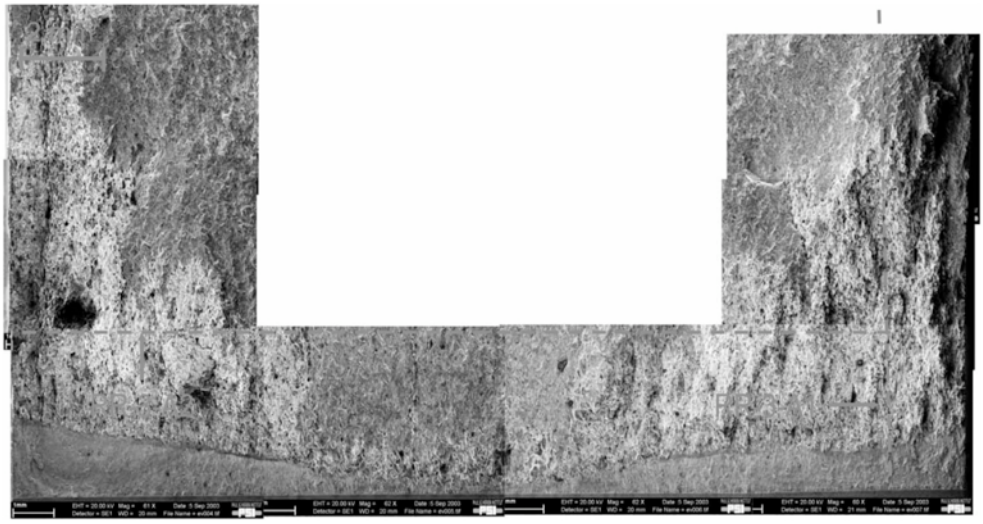

Figure 83. Entire crack surface of Alloy 600 round robin specimen RR-3 tested in PWR water at 320°C.

* H. P. Seifert, Paul Scherrer Institute, Switzerland, private communication to O. K. Chopra, 2003.

Figure 84a shows a more detailed, selected portion of the crack surface. Figures 84b,c are high magnification micrographs showing the boxed areas in Fig. 84a. We observed a morphology with cleavage–like facets and broken planes early in the test (Fig. 84b), followed by an exclusively IG fracture mode (Fig. 84b). Secondary cracks, along a plane parallel to the direction of crack growth but perpendicular to the fracture plane, are visible in the IG fracture region.

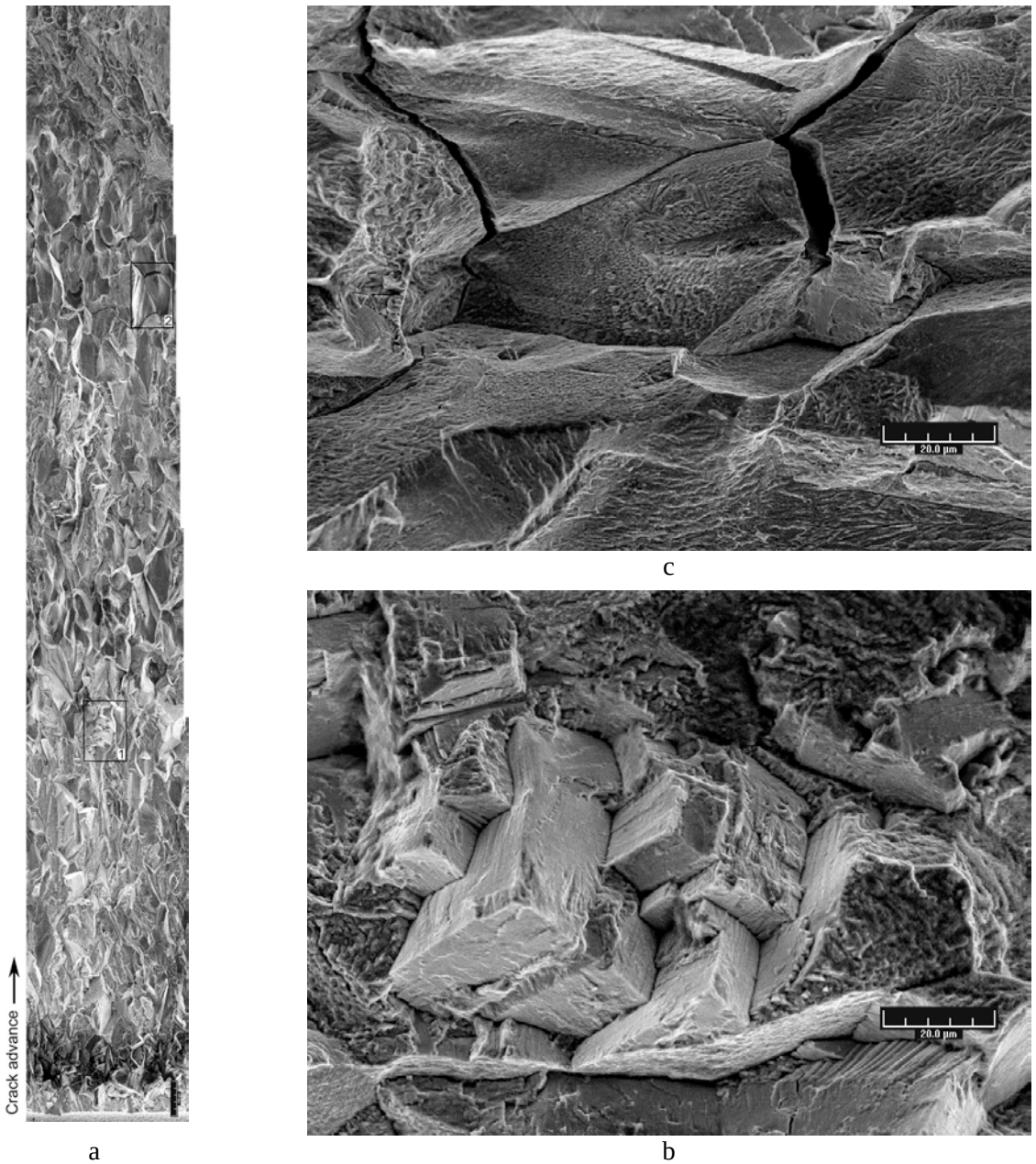

a b c

Figure 84. (a) Selected portion of the crack surface of Alloy 600 round robin specimen RR-1 tested in PWR water at 320°C showing the changes in fracture morphology, and (b,c) micrographs taken at the boxed positions 1 and 2, respectively, in (a).

5.3.2 Alloy 182 Double–J Weld Specimen

The CGR test on Specimen CT31–W01 (TS orientation) of Alloy 182 SMA weld was started in simulated PWR water at 320°C with the water system operating in the recirculating mode at a flow rate of ≈60 cc/min. The system was operated about a week for the environmental conditions to stabilize. The ECPs, measured at 289°C at the exit of the autoclave, of a Alloy 600 sample and Pt electrode were –686 and –690 mV (SHE), respectively; the water system was switched to the once–through mode during ECP measurements to prevent possible contamination of the test solution. The specimen was fatigue precracked at R = 0.3, K_{max} = 23 MPa $m^{1/2}$, triangular waveform, and 0.5 Hz frequency. After ≈0.3–mm extension, R was increased incrementally to 0.7, and the frequency decreased to 0.005 Hz. The experimental conditions and results for the test are given in Table 17; the changes in crack length and K_{max} with time during various test periods are shown in Fig. 85. Note that at 140, 250, 380, and 580 h, the DC potential measurements were not recorded for short periods extending 10–20 h.

The test was interrupted at 407 h and 593 h because of large fluctuations in the system pressure. Again, the problem was identified to be caused by $Al(OH)_3$ deposits in the cooler regions of the water system. The entire return line from the autoclave to the supply feedwater tank including the back–pressure regulator, was replaced or cleaned by back flushing. The test was restarted under the loading conditions prior to the interruption but with the system operating in a once–through mode at a lower flow rate of ≈10 cc/min. In the case of both interruptions, the CGRs existing before the interruption were restored after restart.

After the test, the specimen was fractured in liquid nitrogen. A photomicrograph of the fracture surface of one-half of the specimen is shown in Fig. 86; the crack front is relatively straight. The average crack extension for the transgranular region and the total crack advance were determined by taking ≈20 measurements across the width of the specimen. The measured total crack extension was greater than the value determined from the DC potential measurements, most likely because of several unbroken ligaments in the intergranular region. Thus, the transgranular data was not corrected, and a factor 2.1 was applied to the DC potential data for the intergranular region; the corrected data are given in Table 17.

Table 17. Crack growth data for specimen CT31-W01 TS of Alloy 182 SMA weld in PWR water[a] at 320°C.

Test Period	Test Time, h	Conduc-tivity,[b] µS/cm	O_2 Conc.,[b] ppb	Load Ratio R	Rise Time, S	Down Time, s	Hold Time, s	K_{max}, MPa·$m^{1/2}$	ΔK, MPa·$m^{1/2}$	CGR_{env}, m/s	Estimated CGR_{air}, m/s	Crack Length, mm
1	25	25.0	<10	0.3	1	1	0	23.22	16.25	5.62E-08	1.55E-08	12.976
2	40	25.0	<10	0.3	10	10	0	24.00	16.80	1.72E-08	1.78E-09	13.523
3	90	25.0	<10	0.6	10	10	0	23.86	9.55	1.94E-09	4.17E-10	13.718
4a	135	25.3	<10	0.7	10	10	0	24.64	7.39	1.59E-09	2.15E-10	13.832
4b	281	25.3	<10	0.7	10	10	0	25.26	7.58	1.26E-09	2.38E-10	14.371
5	407	24.4	<10	0.7	100	100	0	25.43	7.63	2.55E-10	2.45E-11	14.394
6	498	23.9	<10	0.7	100	100	0	25.59	7.68	2.73E-10	2.52E-11	14.497
7	552	22.7	<10	0.7	500	500	0	25.57	7.67	negligible	5.02E-12	14.497
8	593	23.0	<10	0.7	1000	12	0	28.55	8.56	2.40E-10	3.94E-12	14.588
9	858	20.0	<10	0.7	1000	12	0	28.86	8.66	5.25E-11	4.12E-12	14.687
10	1214	20.5	<10	0.7	1000	12	3600	29.03	8.71	9.79E-11[c]	4.22E-12	14.790

[a]Simulated PWR water with 2 ppm Li, 1100 ppm B, and 2 ppm dissolved hydrogen (≈23 cc/kg).
[b]Represents values in the effluent; conductivity was ≈21.5 µS/cm in feedwater.
[c]Represents the SCC component of the CGR; average CGR for the period was 5.93 x 10^{-11} m/s.

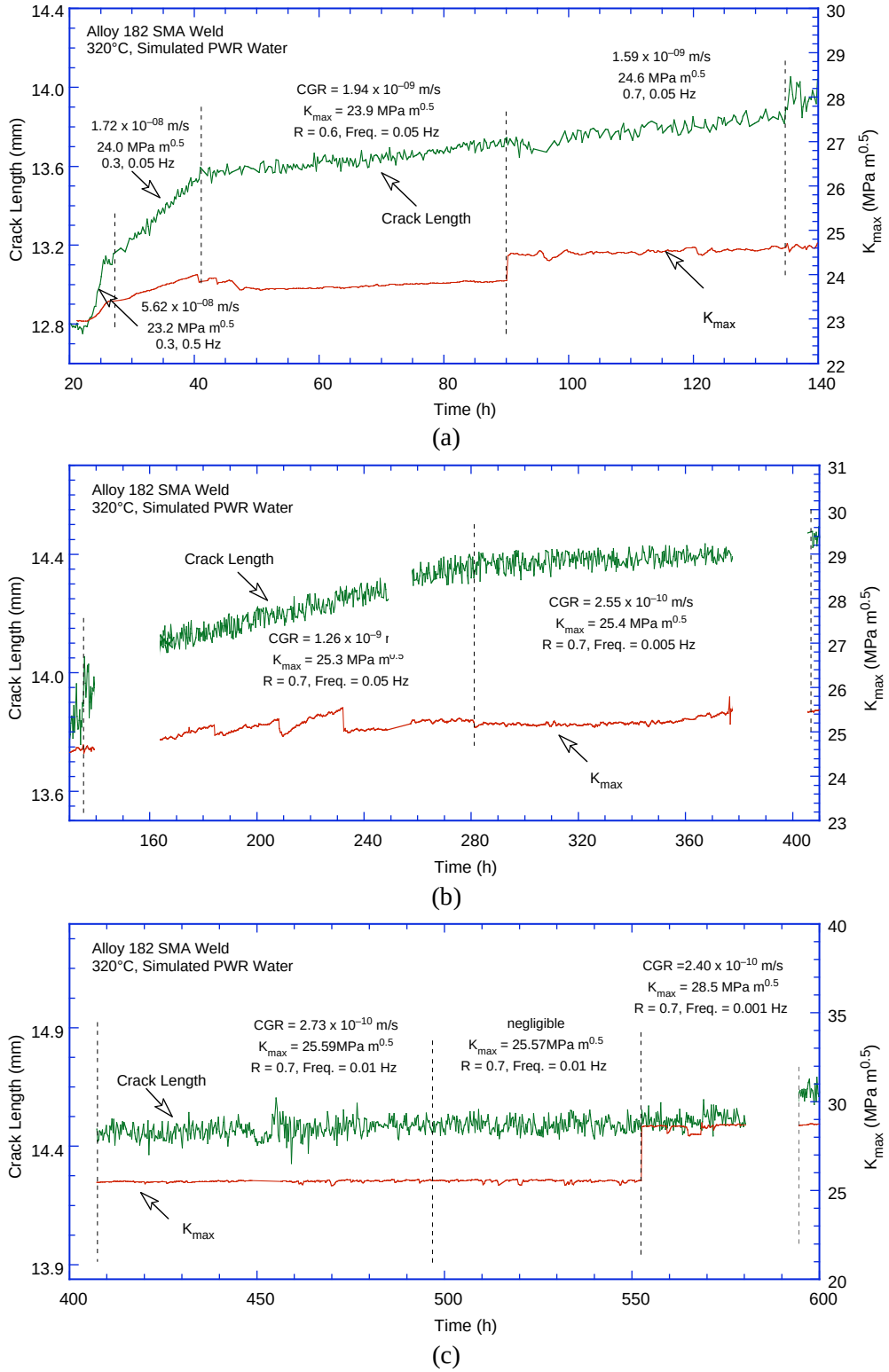

Figure 85. Crack length vs. time plot for Alloy 182 SMA weld–metal specimen in simulated PWR environment at 320°C during test periods (a) 1–4a, (b) 4b-5, (c) 6-8, (d) 9, and (e) 10.

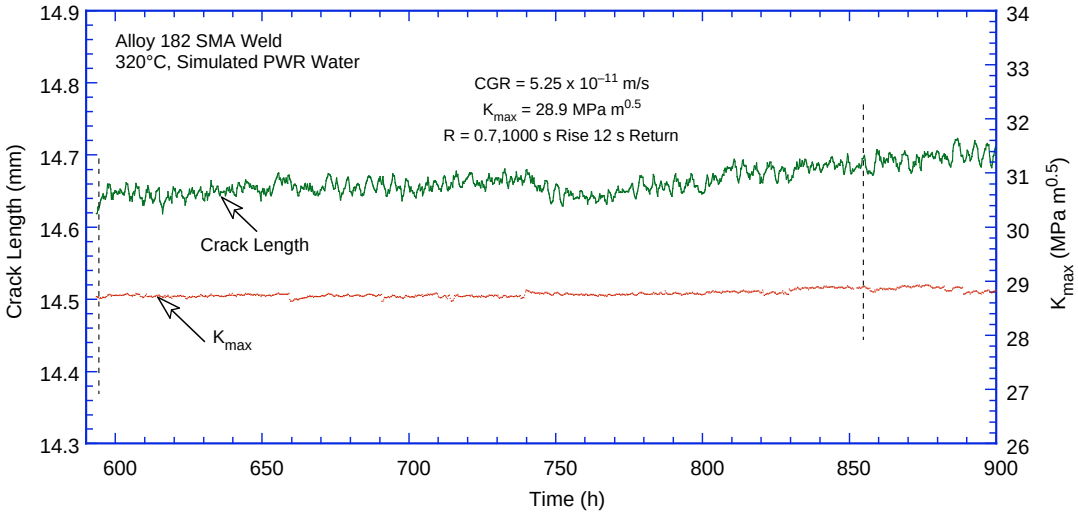

(d)

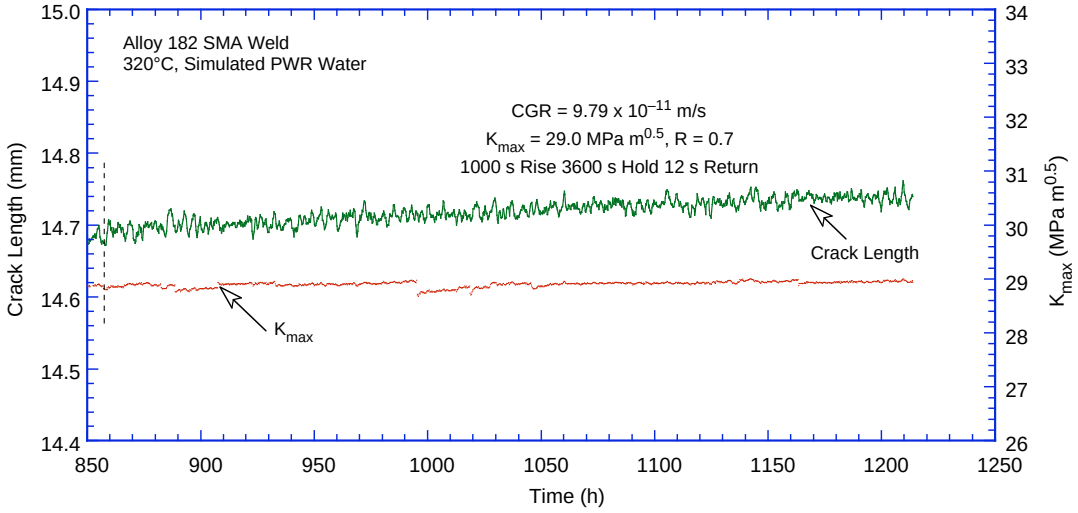

(e)

Figure 85. (Contd.)

To correlate different fracture modes with the test parameters (Table 17), the fracture surface of the specimen was also investigated by high magnification SEM. Figure 87a is a collage of micrographs showing the entire crack extension in a region corresponding to the boxed area of Fig. 86. High magnification micrographs of locations designated 3, 2, and 1 in Fig. 87a are shown in Figs. 87b, c, and d, respectively.

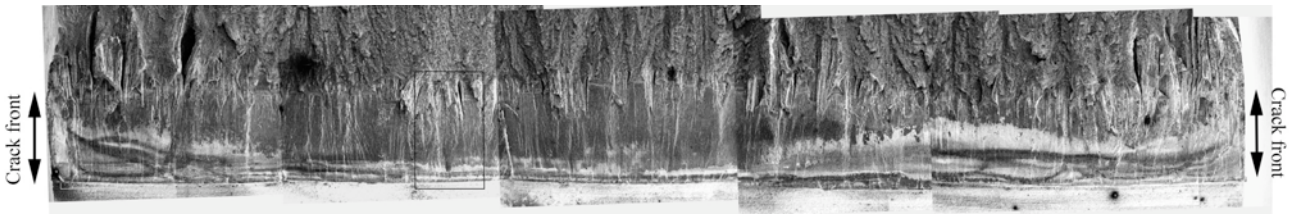

Figure 86. Photomicrograph of the fracture surface of specimen CT31-W01.

The results indicate that cracking initiated and progressed in a transgranular (TG) mode along the columnar grains and through the dendritic microstructure up to approximately 1300-1400 μm. At longer crack extensions, the fracture mode is predominantly intergranular (IG) with significant secondary IG cracks parallel to the direction of crack advance (Fig. 87a). Table 17 indicates that the change to an IG fracture mode occurred during test period 5 when the rise time was increased from 10 to 100 s. Nevertheless, secondary IG cracks apparently are observed quite early during the test (Figs. 87a and d), but, as shown later in this section, evidence suggests that the secondary IG cracking most likely occurred during the high rise–time testing and extended back into the already cracked region. Figure 87c (location "2" in Fig. 87a) is a high magnification micrograph from the area corresponding to the high rise time testing, and shows the highly deformed facet of an IG crack. Further, close to the end of the crack front, Fig. 87b (location "3" in Fig. 87a) shows a TG stepped fracture surface.

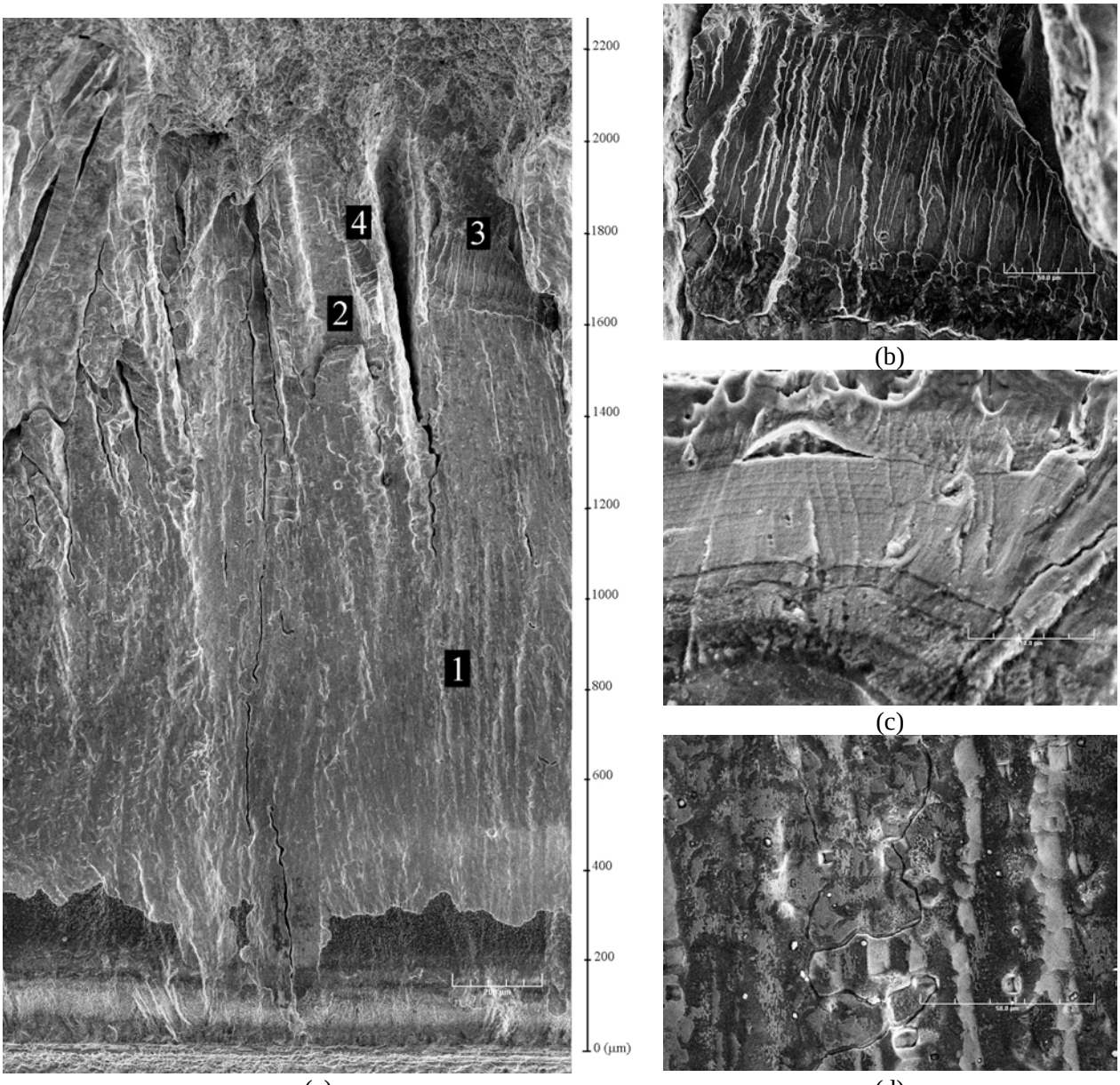

Figure 87. A higher magnification photomicrograph showing entire crack extension in a region in the center of the specimen.

The transition from TG to IG fracture is shown in Fig. 88a. The top–center brighter area of the figure shows IG cracks with the dendrites oriented perpendicular to the direction of crack advance, whereas the adjacent grain with the dendrites oriented parallel to the direction of crack advance shows TG fracture. The existing CGR data for Ni-alloy welds indicate that in PWR environments, the growth rates parallel to the columnar grain structure (T–S orientation) are generally a factor of two greater than those perpendicular to the columnar grain structure (T–L orientation). This conclusion may not be true in all cases. The onset of IG cracking seems to have occurred sooner for the perpendicular grains.

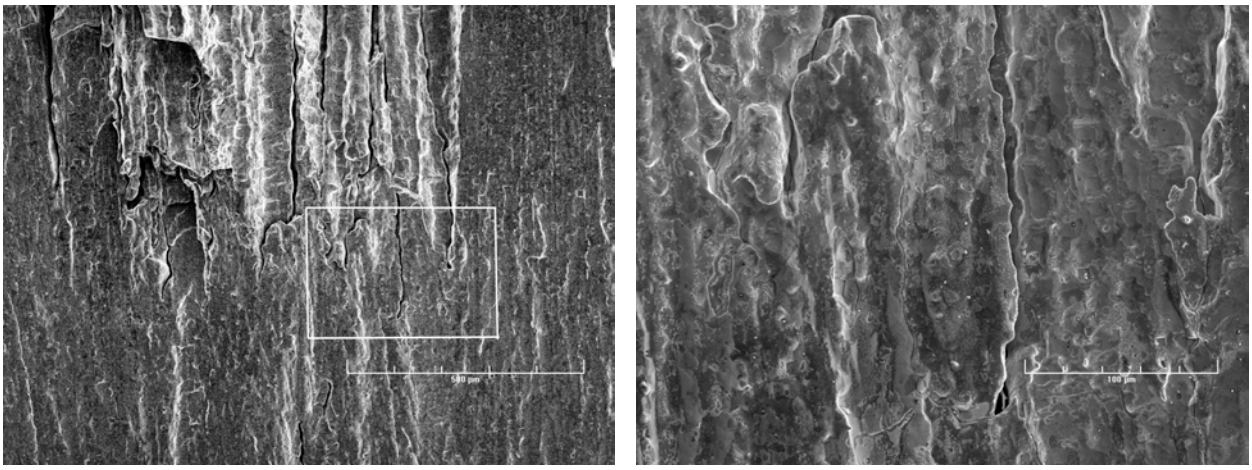

a b

Figure 88. (a) Transition from TG to IG fracture and (b) higher magnification micrograph of the boxed area showing the tip of a few cracks.

Another significant observation concerns the apparent formation of secondary IG cracks quite early during the test. A few examples are shown in the boxed area of Fig. 88a, and at higher magnification in Fig. 88b. The cracks seem to blunt in the TG region, suggesting that they had actually originated in the IG region and propagated back into the TG region. This behavior is substantiated further by additional micrographs in Fig. 89.

Figure 89a identifies an area in the TG region where IG cracks were observed (boxed area). A high magnification micrograph of the region is shown in Fig. 89b, where the two most prominent cracks are designated “1” and “2”. The two cracks appear to shrink as they advance in the TG region, and furthermore, the tips appear blunt (Figs. 89c and d). Such observations lend further support to the hypothesis that the secondary IG cracks most likely originated in the IG region and propagated opposite to the direction of crack advance into the TG region.

The next two sets of micrographs focus on the region obtained near the end of the test during test periods with a hold time and/or a high rise–time. As mentioned earlier the crack extension measured after the test was ≈35% greater than that determined by the DC potential measurements. The present results indicate that the crack front might have advanced in a non–uniform manner, faster along some grain orientations, leaving behind more–resistant, unbroken ligaments. In turn these ligaments would cause the DC potential technique to underestimate the crack length. The first set of micrographs (Figs. 90) show two examples where ductile fracture is adjacent to IG cracking. The high magnification micrographs (Figs. 90b, d) were obtained at the positions indicated by arrows in Figs. 90a and c. It thus appears very likely that some IG crack fronts propagated independently of each other, and the unbroken ligament ruptured when the specimen was fractured in air.

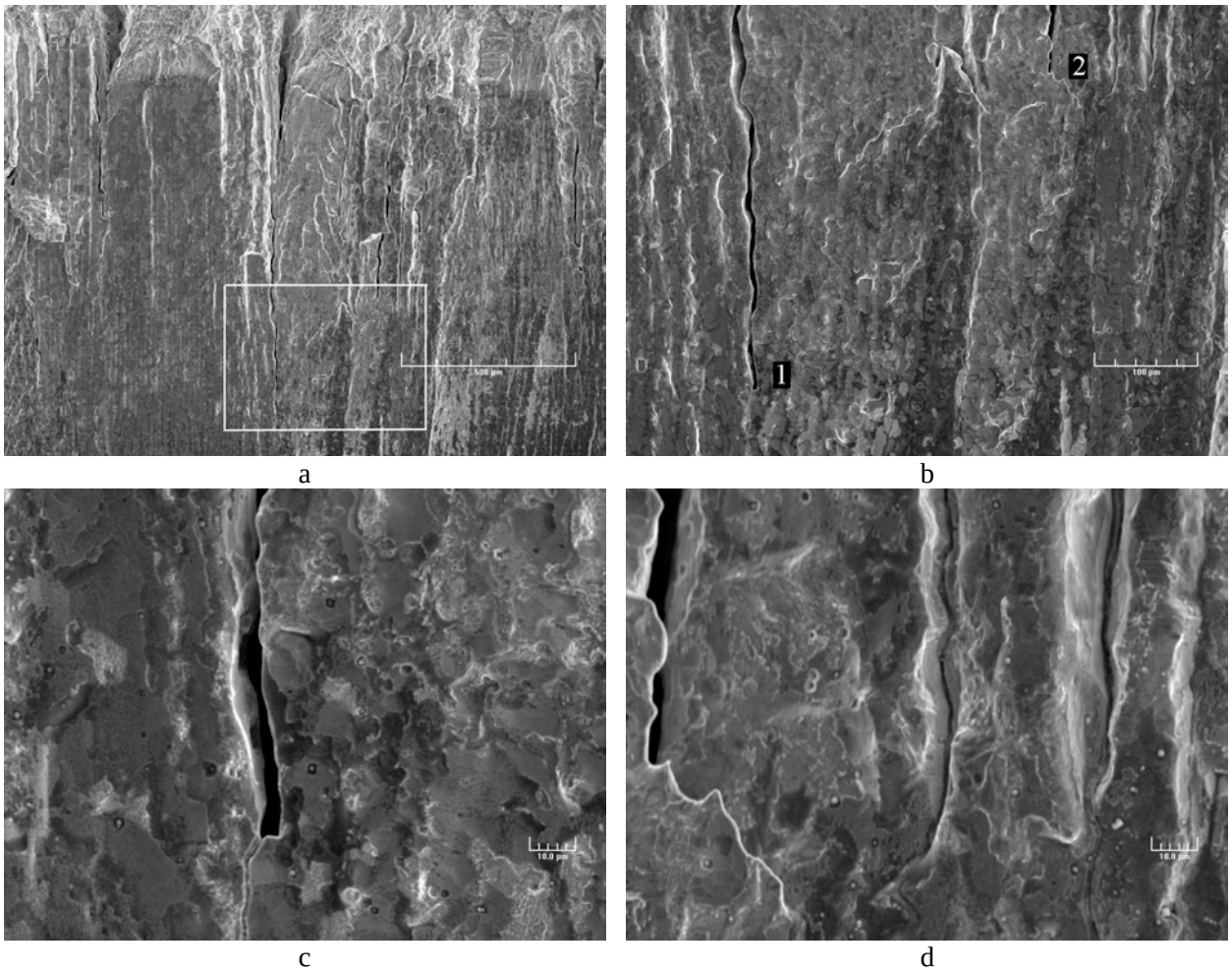

Figure 89. (a) Mixed TG and IG fracture modes, (b) high magnification micrograph of the boxed area, and (c,d) micrographs showing the crack tips at locations “1” and “2.”

By contrast, the second set of micrographs, Fig. 91, documents cases of various TG fracture morphologies observed in the last test region. These show examples of stepped TG (Figs. 91a, b) and cleavage with steps and crack arrest markings (Figs. 91c, d). These cases of TG in a test condition favoring IG are probably similar to those described in Fig. 90, i.e., grains of unfavorable orientation for crack advance situated between two faster propagating regions. It can thus be envisaged that high local stresses combined with the effect of environment caused these grains to crack in a TG mode.

In summary, the examination of the fracture surface of the CT31-W01 TS specimen revealed that the fracture mode correlates well with the testing condition. Specifically, high rise times or long hold periods favor IGSSC. Also, IG cracking apparently advanced more readily along some grain orientations than others, resulting in a crack front with occasional unbroken ligaments and few regions of TG cracking.

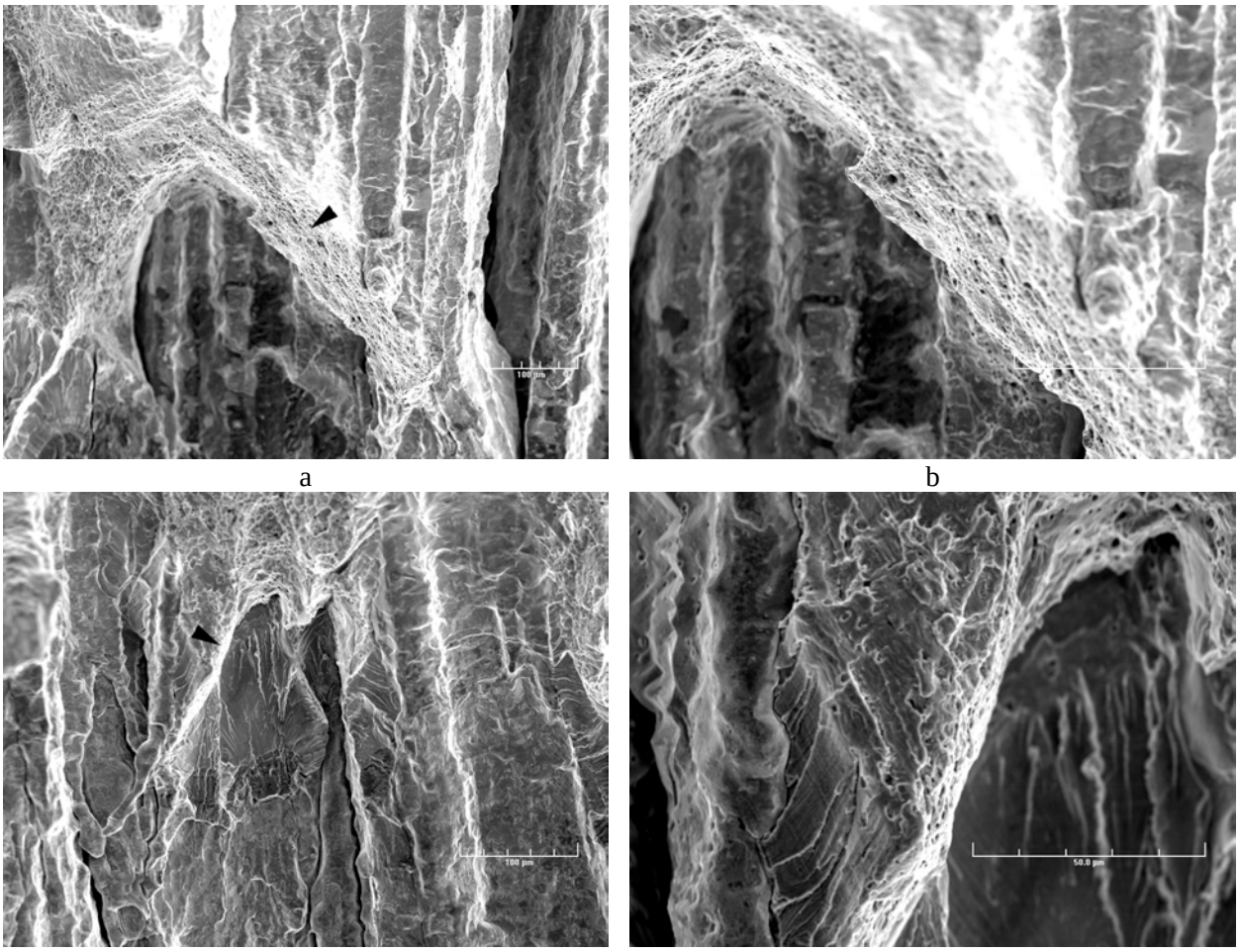

a b

c d

Figure 90. (a,c) Photomicrographs detailing the fracture in a region during test periods with a hold time and/or a high rise time, and (b,d) high magnification micrographs of positions indicated by arrows.

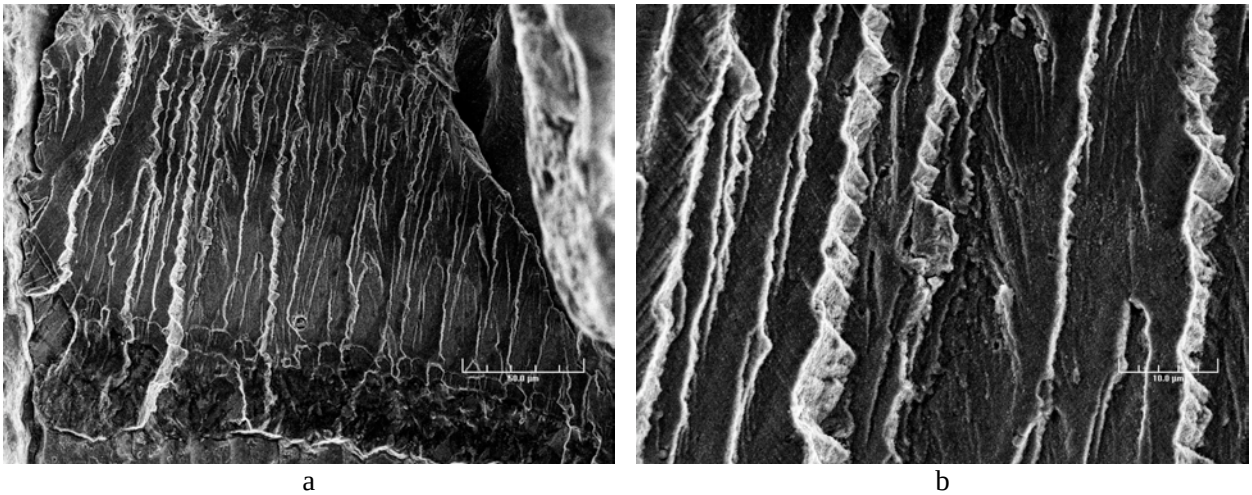

a b

Figure 91. (a,c) Photomicrographs detailing the fracture in a region during test periods with a hold time and/or a high rise time, and (b,d) high magnification micrographs.

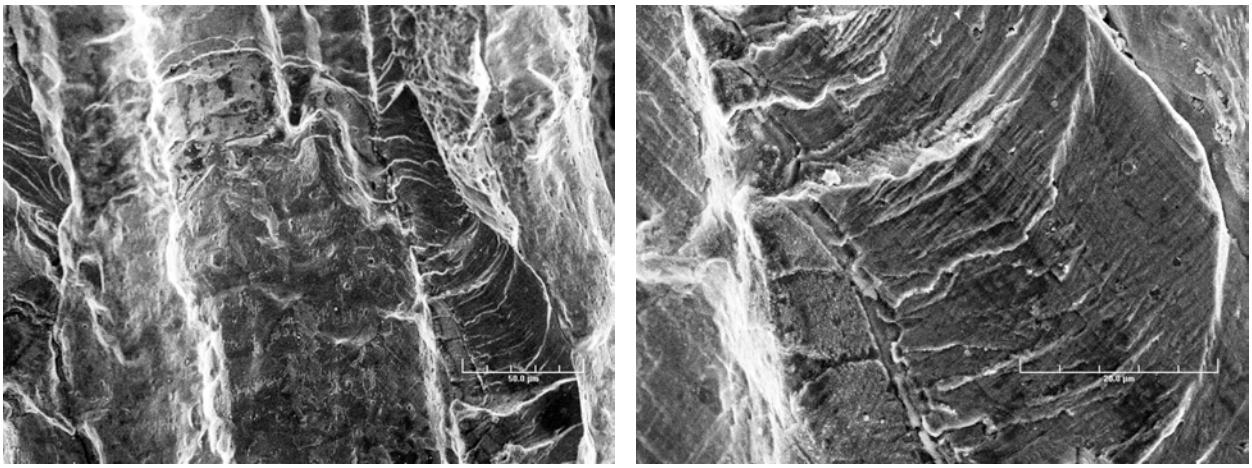

c d

Figure 91. (Continued)

The experimental CGRs obtained under cyclic loading and those predicted in air for Alloy 600 (i.e., calculated from Eq. 11) under the same loading conditions are plotted in Fig. 92. Most of the results follow a line parallel to the diagonal in the figure, indicating that, in air, the cyclic CGRs of the Alloy 182 weld metal are a factor of ≈5 higher than those of Alloy 600. Some environmental enhancement of CGRs is observed in the PWR environment during test periods 6–9, i.e., at R = 0.7 and very low frequencies.

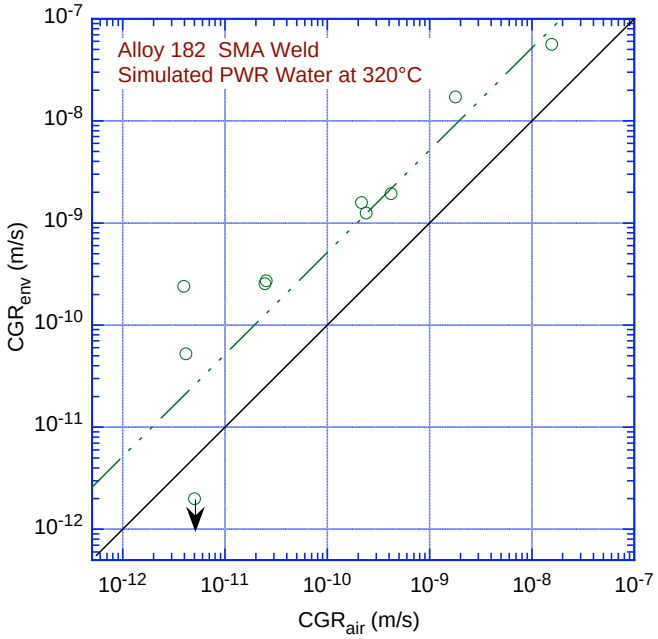

Figure 92.
CGR data for Alloy 182 SMA weld–metal specimen in simulated PWR environment at 320°C.

The experimental CGRs obtained with a trapezoidal waveform (i.e., essentially a constant load with periodic unload/reload) are compared with available CGR data for Ni–alloy welds[107–114] in Fig. 93. The CGR disposition curve, based on the Scott model for Alloy 182[114] in the PWR environment at 325°C, is also plotted in the figure. The data were normalized to 325°C using the K dependency of the Scott model and an activation energy of 130 kJ/mole. The growth rate for the ANL weld is close to the average behavior for Alloy 600. Most of the existing data for Alloy 182 and 82 welds are between the Alloy 600 average curve and a factor of 10 above this curve.

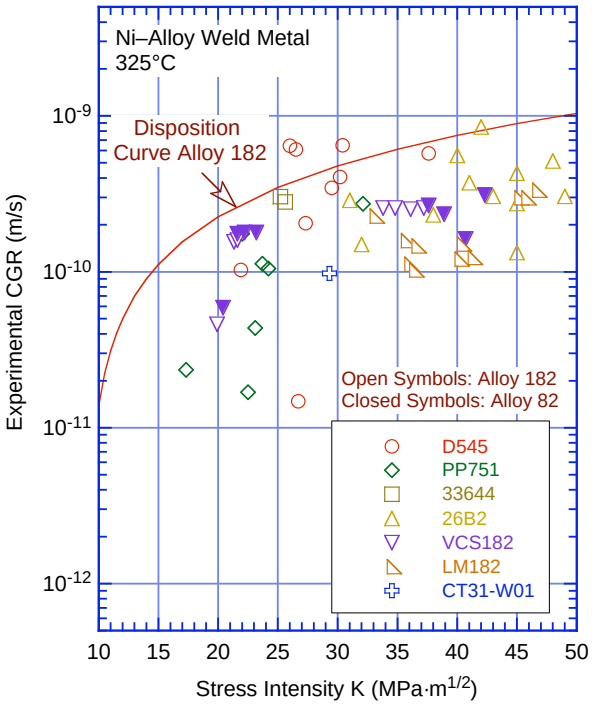

Figure 93.
Comparison of the SCC growth rate for the Argonne Alloy 182 weld with the available data for Alloy 182 and 82 welds in simulated PWR environment. All results normalized to 325°C using an activation energy of 130 kJ/mole.
Data from Refs. 107–114.

6 Summary

6.1 Environmental Effects on Fatigue ε–N Behavior

Fatigue tests have been conducted on two heats of Type 304 SS under various material conditions to determine the effect of heat treatment on fatigue crack initiation in these steels in air and LWR environments. A detailed metallographic examination of fatigue test specimens was performed, with special attention to crack morphology at the sites of initiation, the fracture surface, and the occurrence of striations.

The results indicate that heat treatment has little or no effect on the fatigue life of Type 304 SS in air and low–DO PWR environments. In a high–DO BWR environment, fatigue life is lower for sensitized SSs; life continues to decrease as the degree of sensitization is increased. The cyclic strain–hardening behavior of Type 304 SS under various heat treatment conditions is identical; only the fatigue life varies in different environments.

In air, irrespective of the degree of sensitization, the fracture mode for crack initiation (crack lengths up to ≈200 μm) and crack propagation (crack lengths >200 μm) is transgranular (TG), most likely along crystallographic planes, leaving behind relatively smooth facets. With increasing degree of sensitization, cleavage–like or stepped TG fracture, and occasionally ridge structures on the smooth surfaces were observed. In the BWR environment, the initial crack appeared intergranular (IG) for all heat–treatment conditions, implying a weakening of the grain boundaries. For all four conditions tested, the initial IG mode transformed within 200 μm into a TG mode with cleavage–like features. It appears, however, that the size of the IG portion of the crack surface increased with the degree of sensitization. By contrast, for all of the samples tested in PWR environments, the cracks initiated and propagated in a TG mode irrespective of the degree of sensitization. Prominent features of all fracture surfaces in the PWR case were highly angular, cleavage–like fracture facets that exhibited well–defined "river" patterns. Intergranular facets were rarely observed, but those that were found were mostly in the more heavily sensitized alloys.

Fatigue striations normal to the crack advance direction were clearly visible beyond ≈200 μm on the fracture surfaces for all material and environmental conditions. Striations were found on both the TG and IG facets of the samples tested in BWR conditions, or co-existing with the "river" patterns specific to the samples tested in the PWR environment. Evidence of extensive rubbing due to repeated contact between the two mating surfaces was also found.

The orientation of the cracks as they initiated at the specimen surface was also a function of the test environment. For air tests, cracks initiated obliquely, approaching 45°, with respect to the tensile axis. By contrast, for tests in either the BWR or PWR environment cracks tended to initiate perpendicular to the tensile axis. In all environments, the overall orientation of the crack became perpendicular to the tensile axis as the crack grew beyond the initiation stage.

6.2 Irradiation–Assisted Stress Corrosion Cracking of Austenitic Stainless Steel in BWRs

Slow-strain-rate tensile tests were conducted in high-purity 289°C water on steels irradiated to ≈0.43, 1.3, and 3.0 dpa in helium in the Halden Reactor. The bulk S content provided the best and the only good correlation with the susceptibility to IGSCC in 289°C water. Good resistance to IASCC was

observed in Type 304 and 316 steels that contain very low concentrations of S of ≈0.002 wt.% or less. The IASCC susceptibility of Type 304, 304L, 316, and 316L steels that contain >0.003 wt.% S increased drastically. Steels containing ≥0.008 wt.% were very susceptible at high fluence. These observations indicate that the deleterious effect of S plays a dominant role in the failure of core internal components at high fluence.

In contrast to Type 304 and 316 SSs, a low concentration of S of ≈0.001-0.002 wt.% does not necessarily render low-C Type 304L and 316L, or high-purity-grade steel resistant to IASCC. This finding indicates that a high concentration of C is beneficial in reducing the deleterious effect of S, and that the threshold S concentration to ensure good IASCC resistance is lower in a low-C steel than in a high-C steel.

A comparison of the results with data available in the literature is presented. The IASCC–resistant or –susceptible behavior of austenitic SSs in BWR-like oxidizing environment is represented in terms of a two–dimensional map of bulk S and C contents of the steels. To investigate the importance of the roles of S and C on IASCC, evidence of grain-boundary segregation was characterized by Auger electron spectroscopy on BWR neutron absorber tubes fabricated from two heats of Type 304 SS.

Crack growth tests have been performed in simulated BWR environments at ≈289°C on austenitic SS base metal and weld HAZ specimens irradiated up to 2.0×10^{21} n/cm^2 (3 dpa) at ≈288°C in a helium environment. The tests were conducted under cyclic loading with a slow/fast sawtooth waveform and long rise times or a trapezoidal waveform. The CGR data were obtained on Type 304L SS (Heat C3) irradiated to 0.3×10^{21} n/cm^2, nonirradiated Type 304L SS weld HAZ from the GG reactor core shroud, and a Type 304 SS SS laboratory–prepared weld.

Type 304L irradiated to 0.3×10^{21} n/cm^2 showed very little enhancement of CGRs in high–DO water. Under cyclic loading, the CGRs may be represented by the Shack/Kassner model for nonirradiated austenitic SSs in high–purity water with 0.2 ppm DO. Under constant load, the CGRs were below the NUREG–0313 disposition curve for sensitized SSs in water with 8 ppm DO.

The results for the weld HAZ material indicate that under loading conditions that resulted in predominantly mechanical fatigue (i.e., no environmental enhancement), experimental CGRs for the GG Type 304L weld HAZ are lower than those for the Type 304 SMA weld HAZ. The CGRs for Type 304 weld HAZ are consistent, and those for the GG weld HAZ are a factor of ≈2 lower than those predicted for austenitic SSs in air. In the high–DO BWR environment (i.e., with environmental enhancement), the cyclic CGRs of Type 304 SS SMA weld HAZ are comparable to those of the GG Type 304L SA weld HAZ. For either the GG or the laboratory–prepared weld HAZ, the growth rates of the thermally treated condition are marginally higher than those of the as–welded condition.

Under constant load, the CGRs of as–welded and as–welded plus thermally treated GG weld HAZ are comparable. For both conditions, the CGRs are a factor of ≈2 lower than the NUREG–0313 curve for sensitized SSs in water with 8 ppm DO. For the thermally treated condition, the CGR of the Type 304 SS weld HAZ is a factor of ≈10 higher than that for the Type 304L weld HAZ.

6.3 Irradiation–Assisted Cracking of Austenitic Stainless Steel in PWRs

A comprehensive irradiation experiment in the BOR-60 Reactor is underway to obtain a large number of tensile and disk specimens irradiated to 5, 10, and 40 dpa under PWR-like conditions at ≈325°C. Irradiation to ≈5 and ≈10 dpa has been completed. The specimens have been transported to

Westinghouse hot cell trough Studsvik. Westinghouse is performing the work to separate and repackage ANL specimens from the CIR and industry specimens. The ANL specimens are expected in August 2004.

Tests performed on the materials irradiated in the Halden BWR reactor may, however, give some insight into potential mechanisms for IASCC that is also relevant to PWRs. After exposure to the conditions of the SSRT test in BWR water, susceptibility to intergranular cracking in an inert environment was determined by rapid bending in air at 23°C. Similar tests were also performed on hydrogen-charged specimens in vacuum. Both types of bend fracture exhibited similar characteristics, suggesting that in both cases hydrogen-induced intergranular failure occurred. However, steels that showed high susceptibility to IGSCC in 289°C water exhibited low susceptibility to intergranular cracking in the tests at 23°C air or vacuum, and vice versa. This finding indicates that although intergranular cracking in 23°C is dominated by H-induced embrittlement of ordinary grain boundaries, other processes control IASCC in 289°C water.

On the basis of this investigation, and studies on binary Ni–S and crack-tip microstructural characteristics of LWR core internal components reported in the literature, an initial IASCC model based on a crack-tip grain-boundary process that involves S has been proposed. In this model, several factors play key roles: grain-boundary segregation of Ni and S, formation of grain-boundary oxide in front of crack tip, formation of Ni– and S–rich thin films, formation of islands between the oxide and metal matrix, and disorder–induced melting or amorphization of the Ni–S thin films and islands at sufficiently high concentration of S.

6.4 Cracking of Nickel Alloys and Welds

The resistance of Ni alloys to EAC in simulated LWR environments is being evaluated. Crack growth tests are being conducted to establish the effects of alloy chemistry, material heat treatment, cold work, temperature, load ratio R, stress intensity K, and DO level on the CGRs of Ni alloys. During this reporting period, CGR tests in simulated PWR environments at 320°C were completed on Alloy 600 from the round robin and Alloy 182 SMA weld metal. The results were compared with the existing CGR data for Ni–alloy welds to determine the relative susceptibility of the specific Ni–alloy weld to environmentally enhanced cracking under a variety of loading conditions. Detailed metallographic examinations to characterize the microstructure of the weld metal are presented.

A CGR test was conducted on a specimen of Alloy 182 SMA weld in TS orientation in simulated PWR water at 320°C. The experimental CGRs obtained under cyclic loading were found to be approximately a factor of 5 higher than for Alloy 600 under the same loading conditions; however, for this Alloy 182 weld metal, little or no environmental enhancement in PWR environment occured. The experimental CGRs obtained with a trapezoidal waveform (essentially a constant load with periodic unload/reload) were compared with the available CGR data from the literature and with the CGR curve based on the Scott model, proposed in PWRMRP–21 for Alloy 182. The growth rate for the specimen tested at ANL agreed well with the available data for welds and was found to be close to the average behavior of Alloy 600. The CGR test was complemented by an extensive examination of the fracture surface conducted with the objective of correlating the test parameters to the resultant fracture modes. The analysis has found that cracking initiated in a TG mode and transitioned to an IG mode during long rise time testing. This testing approach also resulted in an uniform, straight crack front. Another potentially important observation was that the fracture mode was affected by grain orientation. Specifically, IG cracking began more readily along grains having the dendrites parallel to the crack front than on grains having the dendrites perpendicular to the crack front. This orientation-dependent crack

growth was also the cause of the unbroken ligaments left behind, which in turn, caused the DC potential technique to underestimate the crack length.

A CGR test was conducted on an Alloy 600 round–robin specimen in the simulated PWR environment at 320°C according to the testing protocol agreed upon by the CIR group. The resultant CGR data under cyclic loading indicate that for high growth rates, the rates measured for the round robin specimen are a factor of ≈2 lower than those predicted in air. The difference, most likely, is due to the material condition; the round robin specimen was 30% cold worked, whereas the material tested air was annealed. For low growth rates, the measured CGR was higher than predicted. Surface examination revealed that the fracture mode was TG near the machine notch, followed by a transition region of highly angular, cleavage–like facets with "river" patterns, which changed to completely IG fracture for the remainder of the test. Also, the crack front was U-shaped, indicating that the crack growth rates were significantly higher near the edge of the specimen than the center. This last observation is consistent with that made by other round-robin participants from France and Switzerland, and suggests that the distribution of cold work was not uniform across the specimen thickness.

During the reporting period, an OIM analysis of the weld microstructure was also initiated. These initial results indicate that weld alloys contain relatively high proportions of cracking-susceptible random boundaries. In addition, OIM imaging revealed that the weld microstructure consists of clusters of grains sharing similar orientations. The implication of this finding is that weld alloys may contain a class of random boundaries that are be more resistant to cracking when separating grains of similar than different orientations.

References

1. Langer, B. F., "Design of Pressure Vessels for Low–Cycle Fatigue," ASME J. Basic Eng. 84, 389–402 (1962).

2. Criteria of Section III of the ASME Boiler and Pressure Vessel Code for Nuclear Vessels, The American Society of Mechanical Engineers, New York (1964).

3. Chopra, O. K., and W. J. Shack, "Effects of LWR Coolant Environments on Fatigue Design Curves of Carbon and Low–Alloy Steels," NUREG/CR–6583, ANL–97/18 (March 1998).

4. Chopra, O. K., and W. J. Shack, "Environmental Effects on Fatigue Crack Initiation in Piping and Pressure Vessel Steels," NUREG/CR–6717, ANL–00/27 (May 2001).

5. Chopra, O. K., and W. J. Shack, "Review of the Margins for ASME Code Design Curves – Effects of Surface Roughness and Material Variability," NUREG/CR–6815, ANL–02/39 (Sept. 2003).

6. Chopra, O. K., "Effects of LWR Coolant Environments on Fatigue Design Curves of Austenitic Stainless Steels," NUREG/CR–5704, ANL–98/31 (1999).

7. Chopra, O. K., "Mechanisms and Estimation of Fatigue Crack Initiation in Austenitic Stainless Steels in LWR Environments," NUREG/CR–6787, ANL–01/25 (Aug. 2002).

8. Park, J. Y., and W. J. Shack, "Intergranular Crack Propagation Rates in Sensitized Type 304 Stainless Steel in an Oxygenated Water Environment," ANL–83–93 (Dec. 1983).

9. Ruther, W. E., W. K. Soppet, and T. F. Kassner, "Evaluation of Environmental Corrective Actions," Materials Science and Technology Division Light–Water–Reactor Safety Research Program: Quarterly Progress Report, October–December 1983, NUREG/CR–3689 Vol. IV, ANL–83–85 Vol. IV, pp. 51–57 (Aug. 1984).

10. Kanasaki, H., R. Umehara, H. Mizuta, and T. Suyama, "Fatigue Lives of Stainless Steels in PWR Primary Water," Trans. 14th Intl. Conf. on Structural Mechanics in Reactor Technology (SMiRT 14), Lyon, France, pp. 473–483 (1997).

11. Tsutsumi, K., H. Kanasaki, T. Umakoshi, T. Nakamura, S. Urata, H. Mizuta, and S. Nomoto, "Fatigue Life Reduction in PWR Water Environment for Stainless Steels," in Assessment Methodologies for Preventing Failure: Service Experience and Environmental Considerations, PVP Vol. 410-2, R. Mohan, ed., American Society of Mechanical Engineers, New York, pp. 23–34, (2000).

12. Fujiwara, M., T. Endo, and H. Kanasaki, "Strain Rate Effects on the Low–Cycle Fatigue Strength of 304 Stainless Steel in High–Temperature Water Environment; Fatigue Life: Analysis and Prediction," in Proc. Intl. Conf. and Exposition on Fatigue, Corrosion Cracking, Fracture Mechanics, and Failure Analysis, ASM, Metals Park, OH, pp. 309–313 (1986).

13. Higuchi, M., and K. Iida, “Reduction in Low–Cycle Fatigue Life of Austenitic Stainless Steels in High–Temperature Water,” Pressure Vessel and Piping Codes and Standards, PVP Vol. 353, D. P. Jones, B. R. Newton, W. J. O'Donnell, R. Vecchio, G. A. Antaki, D. Bhavani, N. G. Cofie, and G. L. Hollinger, eds., American Society of Mechanical Engineers, New York, pp. 79–86 (1997).

14. Indig, M. E., J. L. Nelson, and G. P. Wozadlo, "Investigation of Protection Potential against IASCC," Proc. 5th Intl. Symp. on Environmental Degradation of Materials in Nuclear Power Systems – Water Reactors, D. Cubicciotti, E. P. Simonen, and R. Gold, eds., American Nuclear Society, LaGrange Park, IL, pp. 941-947 (1992).

15. Kanasaki, H., T. Okubo, I. Satoh, M. Koyama, T. R. Mager, and R. G. Lott, "Fatigue and Stress Corrosion Cracking Behavior of Irradiated Stainless Steels in PWR Primary Water," Proc. 5th Intl. Conf. on Nuclear Engineering, March 26-30, 1997, Nice, France.

16. Kasahara, S., K. Nakata, K. Fukuya, S. Shima, A. J. Jacobs, G. P. Wozadlo, and S. Suzuki, "The Effects of Minor Elements on IASCC Susceptibility in Austenitic Stainless Steels Irradiated with Neutrons," Proc. 6th Intl. Symp. on Environmental Degradation of Materials in Nuclear Power Systems - Water Reactors, R. E. Gold and E. P. Simonen, eds., The Minerals, Metals, and Materials Society, Warrendale, PA, pp. 615-623 (1993).

17. Kodama, M., S. Nishimura, J. Morisawa, S. Shima, S. Suzuki, and M. Yamamoto, "Effects of Fluence and Dissolved Oxygen on IASCC in Austenitic Stainless Steels," Proc. 5th Intl. Symp. on Environmental Degradation of Materials in Nuclear Power Systems – Water Reactors, D. Cubicciotti, E. P. Simonen, and R. Gold, eds., American Nuclear Society, LaGrange Park, IL, pp. 948-954 (1992).

18. Chung, H. M., W. E. Ruther, J. E. Sanecki, A. G. Hins, and T. F. Kassner, "Effects of Water Chemistry on Intergranular Cracking of Irradiated Austenitic Stainless Steels," Proc. 7th Intl. Symp. on Environmental Degradation of Materials in Nuclear Power Systems - Water Reactors, G. Airey et al., eds., NACE International, Houston, pp. 1133-1143 (1995).

19. Jacobs, A. J., G. P. Wozadlo, K. Nakata, T. Yoshida, and I. Masaoka, "Radiation Effects on the Stress Corrosion and Other Selected Properties of Type-304 and Type-316 Stainless Steels," Proc. 3rd Intl. Symp. Environmental Degradation of Materials in Nuclear Power Systems – Water Reactors, G. J. Theus and J. R. Weeks, eds., The Metallurgical Society, Warrendale, PA, pp. 673-680 (1988).

20. Garzarolli, F., D. Alter, P. Dewes, and J. L. Nelson, "Deformability of Austenitic Stainless Steels and Ni–Base Alloys," Proc. 3th Intl. Symp. on Environmental Degradation of Materials in Nuclear Power Systems - Water Reactors, G. J Theus and J. R. Weeks, eds., The Metallurgical Society, Warrendale, PA, pp. 657-664 (1988).

21. Garzarolli, F., P. Dewes, R. Hahn, and J. L. Nelson, "Deformability of High-Purity Stainless Steels and Ni–Base Alloys in the Core of a PWR," Proc. 6th Intl. Symp. on Environmental Degradation of Materials in Nuclear Power Systems - Water Reactors, R. E. Gold and E. P. Simonen, eds., The Minerals, Metals, and Materials Society, Warrendale, PA, pp. 607-613 (1993).

22. Fukuya, K., K. Fuji, M. Nakano, N. Nakajima, and M. Kodama, "Stress Corrosion Cracking on Cold-Worked Stainless Steels Irradiated to High Fluence," Proc. 10th Intl. Conf. on Environmental Degradation of Materials in Nuclear Power Systems - Water Reactors, August 5-9, 2001, Lake Tahoe, Nevada, G. S. Was and J. L. Nelson, eds., NACE International CD-ROM.

23. Chung, H. M., W. E. Ruther, J. E. Sanecki, and T. F. Kassner, "Grain-Boundary Microchemistry and Intergranular Cracking of Irradiated Austenitic Stainless Steels," Proc. 6th Intl. Symp. on Environmental Degradation of Materials in Nuclear Power Systems - Water Reactors, R. E. Gold, and E. P. Simonen, eds., The Minerals, Metals, and Materials Society, Warrendale, PA, pp. 511-519 (1993).

24. Kodama, M., R. Katsura, J. Morisawa, S. Nishimura, S. Suzuki, K. Asano, K. Fukuya, and K. Nakata, "IASCC Susceptibility of Austenitic Stainless Steels Irradiated to High Neutron Fluence," Proc. 6th Intl. Symp. on Environmental Degradation of Materials in Nuclear Power Systems - Water Reactors, R. E. Gold and E. P. Simonen, eds., The Minerals, Metals, and Materials Society, Warrendale, PA, pp. 583-588 (1993).

25. Fukuya, K., K. Nakata, and A. Horie, "An IASCC Study Using High Energy Ion Irradiation," Proc. 5th Intl. Symp. on Environmental Degradation of Materials in Nuclear Power Systems – Water Reactors, August 25-29, 1991, Monterey, CA, D. Cubicciotti, E. P. Simonen, and R. Gold, eds., American Nuclear Society, La Grange Park, IL, 814–820 (1992).

26. Fukuya, K., S. Shima, K. Nakata, S. Kasahara, A. J. Jacobs, G. P. Wozadlo, S. Suzuki, and M. Kitamura, "Mechanical Properties and IASCC Susceptibility in Irradiated Stainless Steels," Proc. 6th Intl. Symp. on Environmental Degradation of Materials in Nuclear Power Systems - Water Reactors, R. E. Gold, and E. P. Simonen, eds., The Minerals, Metals, and Materials Society, Warrendale, PA, pp. 565-572 (1993).

27. Chung, H. M., W. E. Ruther, J. E. Sanecki, A. G. Hins, and T. F. Kassner, "Stress Corrosion Cracking Susceptibility of Irradiated Type 304 Stainless Steels," Effects of Radiation on Materials: 16th Int. Symp., ASTM STP 1175, A. S. Kumar, D. S. Gelles, R. K. Nanstad, and T. A. Little, eds., American Society for Testing and Materials, Philadelphia, pp. 851-869 (1993).

28. Cookson, J. M., D. L. Damcott, G. S. Was, and P. L. Anderson, "The Role of Microchemical and Microstructural Effects in the IASCC of High-Purity Austenitic Stainless Steels," Proc. 6th Intl. Symp. on Environmental Degradation of Materials in Nuclear Power Systems - Water Reactors, R. E. Gold, and E. P. Simonen, eds., The Minerals, Metals, and Materials Society, Warrendale, PA, pp. 573-580 (1993).

29. Jacobs, A. J., G. P. Wozadlo, T. Okada, S. Kawano, K. Nakata, S. Kasahara, and S. Suzuki, "The Correlation of Grain Boundary Composition in Irradiated Stainless Steels with IASCC Resistance," Proc. 6th Intl. Symp. on Environmental Degradation of Materials in Nuclear Power Systems - Water Reactors, R. E. Gold and E. P. Simonen, eds., The Minerals, Metals, and Materials Society, Warrendale, PA, pp. 597-604 (1993).

30. Kodama, M., J. Morisawa, S. Nishimura, K. Asano, S. Shima, and K. Nakata, “Stress Corrosion Cracking and Intergranular Corrosion of Austenitic Stainless Steels Irradiated at 323 K,” J. Nucl. Mater., 212–215, 1509 (1994).

31. Tsukada, T., and Y. Miwa, "Stress Corrosion Cracking of Neutron Irradiated Stainless Steels," Proc. 7th Int. Symp. on Environmental Degradation of Materials in Nuclear Power Systems - Water Reactors, G. Airey et al., eds., NACE International, Houston, pp. 1009–1018 (1995).

32. Tsukada, T., Y. Miwa, H. Nakajima, and T. Kondo, “Effects of Minor Elements on IASCC of Type 316 Model Stainless Steels,” Proc. 8th Int. Symp. on Environmental Degradation of Materials in Nuclear Power Systems - Water Reactors, Aug. 10-14, 1997, Amelia Island, FL, S. M. Bruemmer, ed., American Nuclear Society, La Grange Park, IL, pp. 795-802 (1997).

33. Katsura, S., Y. Ishiyama, N. Yokota, T. Kato, K. Nakata, K. Fukuya, H. Sakamoto, and K. Asano, “Post-Irradiation Annealing Effects of Austenitic SS in IASCC,” Corrosion 98, NACE International, Houston, TX, Paper #0132 (1998).

34. Jenssen, A., and L. G. Ljungberg, "Irradiation-Assisted Stress Corrosion Cracking - Postirradiation CERT Tests of Stainless Steels in a BWR Test Loop," Proc. 7th Intl. Symp. on Environmental Degradation of Materials in Nuclear Power Systems - Water Reactors, G. Airey et al., eds., NACE International, Houston, pp. 1043–1052 (1995).

35. Jenssen, A., P. Efsing, K. Gott, and P.-O. Andersson, “Crack Growth Behavior of Irradiated Type 304L Stainless Steel in Simulated BWR Environment,” in CD, Proc. 11th Intl. Conf. on Environmental Degradation of Materials in Nuclear Power Systems - Water Reactors, Stevenson, WA, Aug. 10-14, pp. 1015-1026 (2003).

36. Tanaka, Y., S. Suzuki, K. Fukuya, H. Sakamoto, M. Kodama, S. Nishimura, K. Nakata, and T. Kato, "IASCC Susceptibility of Type 304, 304L, and 316 Stainless Steels," Proc. 8th Int. Symp. on Environmental Degradation of Materials in Nuclear Power Systems - Water Reactors, S. M. Bruemmer, ed., American Nuclear Society, LaGrange Park, IL, pp. 803-811 (1997).

37. Busby, J. T., and G. S. Was, “Irradiation-Assisted Stress Corrosion Cracking in Model Austenitic Alloys with Solute Additions,” in CD-ROM Proc. 11th Intl. Conf. on Environmental Degradation of Materials in Nuclear Power Systems - Water Reactors, Stevenson, WA, Aug. 10-14, pp. 995-1014 (2003).

38. Karlsen, T. M., and E. Hauso, “Qualification and Application of Instrumented Specimens for In-Core Studies on Cracking Behavior of Austenitic Stainless Steels,” Proc. 9th Intl. Symp. on Environmental Degradation of Materials in Nuclear Power Systems - Water Reactors, August 1-5, 1999, Newport Beach, CA, S. Bruemmer, P. Ford, and G. Was, eds., The Metallurgical Society, Warrendale, PA, pp. 951-961 (1999).

39. Garzarolli, F., P. Dewes, R. Hahn, and J. L. Nelson, "In-Reactor Testing of IASCC Resistant Stainless Steels," Proc. 7th Intl. Symp. on Environmental Degradation of Materials in Nuclear Power Systems - Water Reactors, G. Airey et al., eds., NACE International, Houston, pp. 1055–1065 (1995).

40. Chung, H. M., W. E. Ruther, J. E. Sanecki, A. G. Hins, N. J. Zaluzec, and T. F. Kassner, “Irradiation–Assisted Stress Corrosion Cracking of Austenitic Stainless Steels: Recent Progress and New Approaches,” J. Nucl. Mater. 239, 61 (1996).

41. Chung, H. M., R. V. Strain, and W. J. Shack, "Irradiation-Assisted Stress Corrosion Cracking of Model Austenitic Stainless Steel Alloys," in CD-ROM, Proc. 10th Intl. Conf. on Environmental Degradation of Materials in Nuclear Power Systems - Water Reactors, Lake Tahoe, NV (Aug. 2001).

42. Chung, H. M., R. V. Strain, and R. W. Clark, "Irradiation-Assisted Stress Corrosion Cracking of Austenitic Stainless Steel in BWRs," Environmentally Assisted Cracking in Light Water Reactors, NUREG/CR-4667, Vol. 32, ANL-02/33, Annual Report, Argonne National Laboratory, pp. 19-28 (June 2003).

43. Chung, H. M., R. V. Strain, and R. W. Clark, "Irradiation-Assisted Stress Corrosion Cracking of Austenitic Stainless Steel in BWRs," in Environmentally Assisted Cracking in Light Water Reactors, NUREG/CR-4667, Vol. 33, ANL-03/36, Annual Report, Argonne National Laboratory, pp. 21-33 (2005).

44. Shen, A.-T., and C. S. Chang, "IASCC Behavior of 304L Stainless Steel," in CD-ROM Proc. 11th Intl. Conf. on Environmental Degradation of Materials in Nuclear Power Systems - Water Reactors, Stevenson, WA, Aug. 10-14, pp. 986-994 (2003).

45. Thomas, L. and S. Bruemmer, "Analytical Transmission Microscopy (ATEM) Characterization of Stress Corrosion Cracks in LWR–Irradiated Austenitic Stainless Steel Components," EPRI–1003422, Electric Power Research Institute, Palo Alto, CA (May 2002).

46. Thomas, L. and S. Bruemmer, "Analytical Transmission Microscopy (ATEM) Characterization of Stress Corrosion Cracks in LWR–Irradiated Austenitic Stainless Steel Components," in CD–ROM Proc. 11th Intl. Conf. on Environmental Degradation of Materials in Nuclear Power Systems – Water Reactors, Stevenson, WA, Aug. 10–14, pp. 1049–1061 (2003).

47. Jacobs, A. J., R. E. Clausing, M. K. Miller, and C. Shepherd, "Influence of Grain Boundary Composition on the IASCC Susceptibility of Type 348 Stainless Steel," Proc. 4th Intl. Conf. on Environmental Degradation of Materials in Nuclear Power Systems – Water Reactors, Stevenson, WA, pp. 14–21 to 14–44.

48. Andresen, P. L., and C. L. Briant, "The Role of S, P, and N Segregation in Intergranular Environmental Cracking of Stainless Steels in High-Temperature Water," Proc. 3rd Intl. Symp. Environmental Degradation of Materials in Nuclear Power Systems – Water Reactors, G. J. Theus and J. R. Weeks, eds., The Metallurgical Society, Warrendale, PA, pp. 371-381 (1988).

49. Dumbill, S., "Examination of Stress Corrosion Crack Tip Microstructures in Stainless Steel," SKI Report 01:35, Swedish Nuclear Power Inspectorate (Sept. 2001).

50. Heuer, J. K., P. R. Okamoto, N. Q. Lam, and J. F. Stubbins, "Disorder–Induced Melting in Nickel: Implication to Intergranular Sulfur Embrittlement," J. Nucl. Mater., 301, 129–141 (2002).

51. Bruemmer, S. M., et al., "Critical Issue Reviews for the Understanding and Evaluation of Irradiation–Assisted Stress Corrosion Cracking," EPRI TR–107159, Electric Power Research Institute, Palo Alto, CA (1996).

52. Herrera, M. L., et al., “Evaluation of the Effects of Irradiation on the Fracture Toughness of BWR Internal Components,” Proc. ASME/JSME 4th Intl. Conf. on Nucl. Eng. (ICONE–4) Vol. 5, A. S. Rao, R. M. Duffey, and D. Elias, eds., American Society of Mechanical Engineers, New York, pp. 245–251 (1996).

53. Mills, W. J., “Fracture Toughness of Type 304 and 316 Stainless Steels and their Welds,” Intl. Mater. Rev. 42, 45–82 (1997).

54. Kanasaki, H., I. Satoh, M. Koyama, T. Okubo, T. R. Mager, and R. G. Lott, “Fatigue and Stress Corrosion Cracking Behaviors of Irradiated Stainless Steels in PWR Primary Water,” Proc. 5th Intl. Conf. on Nuclear Engineering, ICONE5-2372, pp. 1–7 (1997).

55. Andresen, P. L., F. P. Ford, S. M. Murphy, and J. M. Perks, “State of Knowledge of Radiation Effects on Environmental Cracking in Light Water Reactor Core Materials,” Proc. 4th Intl. Symp. on Environmental Degradation of Materials in Nuclear Power Systems – Water Reactors, NACE, pp. 1.83–1.121 (1990).

56. Jenssen, A., and L. G. Ljungberg, “Irradiation Assisted Stress Corrosion Cracking of Stainless Alloys in BWR Normal Water Chemistry and Hydrogen Water Chemistry,” Proc. Sixth Intl. Symp. on Environmental Degradation of Materials in Nuclear Power Systems – Water Reactor, R. E. Gold and E. P. Simonen, eds., Minerals, Metals & Materials Society, pp. 547–553 (1993).

57. Brown, K. S., and G. M. Gordon, “Effects of BWR Coolant Chemistry on the Propensity for IGSCC Initiation and Growth in Creviced Reactor Internals Components,” Proc. Third Intl. Symp. on Environmental Degradation of Materials in Nuclear Power Systems – Water Reactor, AIME, pp. 243–248 (1987).

58. Gordon, G. M., and K. S. Brown, “Dependence of Creviced BWR Component IGSCC Behavior on Coolant Chemistry,” Proc. 4th Intl. Symp. on Environmental Degradation of Materials in Nuclear Power Systems – Water Reactor, Daniel Cubicciotti, ed., NACE, pp. 14.46–14.61 (1990).

59. Garzarolli, F., D. Alter, and P. Dewes, “Deformability of Austenitic Stainless Steels and Nickel–Base Alloys in the Core of a Boiling and a Pressurized Water Reactor,” Proc. Intl. Symp. on Environmental Degradation of Materials in Nuclear Power Systems – Water Reactor, ANS, pp. 131–138 (1986).

60. Kodama, M., et al., “IASCC Susceptibility of Austenitic Stainless Steels Irradiated to High Neutron Fluence,” Proc. Sixth Intl. Symp. on Environmental Degradation of Materials in Nuclear Power Systems – Water Reactor, R. E. Gold and E. P. Simonen, eds., Minerals, Metals & Materials Society, pp. 583–588 (1993).

61. Kodama, M., et al., “Effects of Fluence and Dissolved Oxygen on IASCC in Austenitic Stainless Steels,” Proc. Fifth Intl. Symp. on Environmental Degradation of Materials in Nuclear Power Systems – Water Reactor, American Nuclear Society, pp. 948–954 (1991).

62. Clark, W. L., and A. J. Jacobs, “Effect of Radiation Environment on SCC of Austenitic Materials,” Proc. First Intl. Symp. on Environmental Degradation of Materials in Nuclear Power Systems – Water Reactor, NACE, p. 451 (1983).

63. Andresen, P. L., and F. P. Ford, "Irradiation Assisted Stress Corrosion Cracking: From Modeling and Prediction of Laboratory & In–Core Response to Component Life Prediction," Corrosion/95, Paper No. 419, NACE, Houston TX (1995).

64. Jenssen, A., and L. G. Ljungberg, "Irradiation Assisted Stress Corrosion Cracking of Stainless Alloys in BWR Normal Water Chemistry and Hydrogen Water Chemistry," Proc. Sixth Intl. Symp. on Environmental Degradation of Materials in Nuclear Power Systems – Water Reactor, R. E. Gold and E. P. Simonen, eds., Minerals, Metals & Materials Society, pp. 547–553 (1993).

65. Jenssen, A., and L. G. Ljungberg, "Irradiation Assisted Stress Corrosion Cracking: Post Irradiation CERT Tests of Stainless Steels in a BWR Test Loop," Proc. Seventh Intl. Symp. on Environmental Degradation of Materials in Nuclear Power Systems – Water Reactor, G. Airey et al., eds., NACE, pp. 1043–1052 (1995).

66. Gruber, E. E., and O. K. Chopra, "Crack Growth Rate Test of Austenitic Stainless Steels Irradiated in the Halden Reactor," Environmentally Assisted Cracking in Light Water Reactors, Annual Report, January–December 2002, NUREG/CR–4667 Vol. 33, ANL–03/36, pp. 34-43 (2004).

67. Hazelton, W. S., and W. H. Koo, "Technical Report on Material Selection and Processing Guidelines for BWR Coolant Pressure Boundary Piping, Final Report," NUREG–0313, Rev. 2 (1988).

68. Gruber, E. E., and O. K. Chopra, "Fracture Toughness J," Environmentally Assisted Cracking in Light Water Reactors, Annual Report, January–December 2002, NUREG/CR–4667 Vol. 33, ANL–03/36, pp. 34-43, 2004.

69. James, L. A., and D. P. Jones, "Fatigue Crack Growth Correlation for Austenitic Stainless Steels in Air," Proc. Conf. on Predictive Capabilities in Environmentally–Assisted Cracking, PVP Vol. 99, R. Rungta, ed., American Society of Mechanical Engineers, New York, pp. 363–414 (1985).

70. Shack, W. J., and T. F. Kassner, "Review of Environmental Effects on Fatigue Crack Growth of Austenitic Stainless Steels," NUREG/CR–6176, ANL–94/1 (May 1994).

71. Andresen, P. L., "Similarity of Cold Work and Radiation Hardening in Enhancing Yield Strength and SCC Growth of Stainless Steel in Hot Water," Corrosion/02, Paper 02509, NACE (2002).

72. Andresen, P. L., T. M. Angeliu, W. R. Catlin, L. M. Young, and R. M. Horn, "Effect of Deformation on SCC of Unsensitized Stainless Steel," Corrosion/2000, Paper 00203, NACE (2000).

73. Angeliu, T. M., P. L. Andresen, E. Hall, J. A. Sutliff, and S. Sitzman, "Strain and Microstructure Characterization of Austenitic Stainless Steel Weld HAZs," Corrosion/2000, Paper 00186, NACE (2000).

74. Andresen, P. L., T. M. Angeliu, L. M. Young, W. R. Catlin, and R. M. Horn, "Mechanism and Kinetics of SCC in Stainless Steels," Proc. Tenth Intl. Symp. on Environmental Degradation of Materials in Nuclear Power Systems – Water Reactor, NACE (2001).

75. Shogan, R. P., and T. R. Mager, “Susceptibility of Type 316 Stainless Steel to Irradiated–Assisted Stress Corrosion Cracking in a PWR Environment,” Proc. 10th Intl. Conf. on Environmental Degradation of Materials in Nuclear Power Systems - Water Reactors, G. S. Was and J. L. Nelson, eds., August 5-9, 2001, Lake Tahoe, Nevada, NACE International CD-ROM.

76. Ehrnsten, U., et al., “Intergranular Cracking of an Irradiated Ti-stabilized Austenitic Stainless Steel Spacer Grid Sleeve from a VVER-440 Reactor,” Proc. Ninth Intl. Symp. on Environmental Degradation of Materials in Nuclear Power Systems - Water Reactors, Newport Beach, CA, S. Bruemmer, P. Ford, and G. Was, eds., The Metallurgical Society, Warrendale, PA, pp. 941-950 (1999).

77. Scott, P., “An Analysis of Primary Water Stress Corrosion Cracking in PWR Steam Generators,” Proc. of the Specialists Meeting on Operating Experience with Steam Generators, Brussels, Belgium, pp. 5–6 (1991).

78. Cattant, F., “Lessons Learnt from the Examination of Tubes Pulled from Electricite de France Steam Generators,” Nucl. Eng. Des. 168, 241–253 (1997).

79. Diercks, D. R., W. J. Shack, and J. Muscara, “Overview of Steam Generator Tube Degradation and Integrity Issues,” Nucl. Eng. Des. 194, 19–30 (1999).

80. USNRC Information Notice No. 90–10, “Primary Water Stress Corrosion Cracking (PWSCC) of Inconel 600,” Feb. 1990.

81. USNRC Generic Letter 97-01, “Degradation of Control Rod Drive Mechanism and Other Vessel Closure Head Penetrations,” April 1, 1997.

82. Economou, J., A. Assice, F. Cattant, J. Salin, and M. Stindel, “NDE and Metallurgical Examination of Vessel Head Penetrations,” 3rd Intl. Symp. of Fontevraud, Sept. 12–16, 1994.

83. Robinson, M. R., Duke Power Company, “Oconee Unit 1 and Unit 3 Reactor Vessel Head Leakage, Cracking of RV Head Penetrations due to Primary Water Stress Corrosion Cracking,” presented at the NRC Meeting with the NEI EPRI Material Reliability Program Regarding CRDM Nozzle Crackling Issues, Rockville, MD, April 12, 2001.

84. Frye, C. R., T. Alley, M. L. Arey, Jr., and M. R. Robinson, “Cracking in Alloy 600/182 Reactor Vessel Head Penetrations,” PVP–Vol. 437, Service Experience and Failure Assessment Applications ASME 2002, P. S. Lam, ed., American Society of Mechanical Engineers, New York, pp. 171–178 (2002).

85. USNRC Information Notice 2001–05, “Through–Wall Circumferential Cracking of Reactor Pressure Vessel Head Control Rod Driver Mechanism Penetration Nozzle at Oconee Nuclear Station, Unit 3,” April 30, 2001.

86. USNRC Bulletin 2001–01, “Circumferential Cracking of Reactor Pressure Vessel Head Penetration Nozzles,” Aug. 3, 2001.

87. USNRC Information Notice 2000–17, “Crack in Weld Area of Reactor Coolant System Hot Leg Piping at V. C. Summer,” Oct. 18, 2000; Suppl. 1, Nov. 16, 2000; Suppl. 2, Feb. 28, 2001.

88. Jenssen, A., K. Norrgard, J. Lagerstrom, G. Embring, and D. Tice, "Assessment of Cracking in Dissimilar Metal Welds," Proc. of the Tenth Intl. Conf. on Environmental Degradation of Materials in Nuclear Power Systems-Water Reactors, NACE International, Houston, TX (2001).

89. Bennetch, J. I., G. E. Modzelewski, L. L. Spain, and G. V. Rao, "Root Cause Evaluation and Repair of Alloy 82/182 J–Groove Weld Cracking of Reactor Vessel Head Penetrations at North Anna Unit 2," PVP–Vol. 437, Service Experience and Failure Assessment Applications ASME 2002, P. S. Lam, ed., American Society of Mechanical Engineers, New York, pp. 179–185 (2002).

90. USNRC Information Notice 2002–11, "Recent Experience with Degradation of Reactor Pressure Vessel Head," March 12, 2002.

91. USNRC Information Notice 2003–11, "Leakage Found on Bottom–Mounted Instrumentation Nozzles," Aug. 13, 2003; Suppl. 1, Jan. 8, 2004.

92. USNRC Bulletin 2003–02, "Leakage from Reactor Pressure Vessel Lower Head Penetrations and Reactor Coolant Pressure Boundary Integrity," Aug. 21, 2003.

93. Ruther, W. E., W. K. Soppet, and T. F. Kassner, "Corrosion Fatigue of Alloys 600 and 690 in Simulated LWR Environments," NUREG/CR–6383, ANL–95/37 (April 1996).

94. Ruther, W. E., W. K. Soppet, and T. F. Kassner, "Environmentally Assisted Cracking of Alloys 600 and 690 in Simulated LWR Water," in Environmentally Assisted Cracking in Light Water Reactors, Semiannual Report, July 1997–December 1997, NUREG/CR–4667, Vol. 25, ANL–98/18, pp. 42–75 (Sept. 1998).

95. Ruther, W. E., W. K. Soppet, T. F. Kassner, and W. J. Shack, "Environmentally Assisted Cracking of Alloys 600 and 690 in Simulated LWR Water," in Environmentally Assisted Cracking in Light Water Reactors, Semiannual Report, January 1998–July 1998, NUREG/CR–4667, Vol. 26, ANL–98/18, pp. 25–32 (March 1999).

96. Ruther, W. E., W. K. Soppet, T. F. Kassner, and W. J. Shack, "Environmentally Assisted Cracking of Alloys 600 and 690 in Simulated LWR Water," in Environmentally Assisted Cracking in Light Water Reactors, Semiannual Report, July 1998–December 1998, NUREG/CR–4667, Vol. 27, ANL–99/11, pp. 45-54 (October 1999).

97. Soppet, W. K., O. K. Chopra, and W. J. Shack, "Environmentally Assisted Cracking of Alloys 600 and 690 in Simulated LWR Water," in Environmentally Assisted Cracking in Light Water Reactors, Semiannual Report, July 1999–December 1999, NUREG/CR–4667, Vol. 29, ANL–00/23, pp. 39-45 (November 2000).

98. Chopra, O. K., W. K. Soppet, and W. J. Shack, "Effects of Alloy Chemistry, Cold Work, and Water Chemistry on Corrosion Fatigue and Stress Corrosion Cracking of Nickel Alloys and Welds," NUREG/CR–6721, ANL–01/07 (April 2001).

99. Cassagne, T. B., and A. Gelpi, "Crack Growth Rate Measurements on Alloy 600 Steam Generator Tubes in Steam and Primary Water," Proc. of the Fifth Intl. Symp. on Environmental Degradation of Materials in Nuclear Power Systems-Water Reactors, American Nuclear Society, La Grange Park, IL, pp. 518–524 (1991).

100. Foster, J. P., W. H. Bamford, and R. S. Pathania, “Initial Results of Alloy 600 Crack Growth Rate Testing in a PWR Environment,” Proc. of the Seventh Intl. Symp. on Environmental Degradation of Materials in Nuclear Power Systems-Water Reactors, NACE International, Houston, TX, pp. 25–39 (1995).

101. Magdowski, R., F. Vaillant, C. Amzallag, and M. O. Speidel, “Stress Corrosion Crack Growth Rates of Alloy 600 in Simulated PWR Coolant,” Proc. of the 8th Intl. Symp. on Environmental Degradation of Materials in Nuclear Power Systems-Water Reactors, S. M. Bruemmer, ed., American Nuclear Society, La Grange Park, IL, pp. 333–338 (1997).

102. Le Hong, S., C. Amzallag, and A. Gelpi, “Modeling of Stress Corrosion Crack Initiation on Alloy 600 in Primary Water of PWRs,” Proc. of the Ninth Intl. Symp. on Environmental Degradation of Materials in Nuclear Power Systems-Water Reactors, F. P. Ford, S. M. Bruemmer, and G. S. Was, eds., The Minerals, Metals, and Materials Society, Warrendale, PA, pp. 115–122 (1999).

103. Raquet, O., and G. Santarini, “Stress Corrosion Crack Propagation Rate of Alloy 600 in the Primary Water of PWR Influence of a Cold Worked Layer,” Proc. of the Ninth Intl. Symp. on Environmental Degradation of Materials in Nuclear Power Systems-Water Reactors, F. P. Ford, S. M. Bruemmer, and G. S. Was, eds., The Minerals, Metals, and Materials Society, Warrendale, PA, pp. 207–213 (1999).

104. “Materials Reliability Program (MRP) Crack Growth Rates for Evaluating Primary Water Stress Corrosion Cracking (PWSCC) of Thick–Wall Alloy 600 Material”, MRP–55, EPRI, Licensed Document, Electric Power Research Institute, Palo Alto (2002).

105. Andresen, P. L., and P. G. Campbell, “The Effects of Crack Closure in High–Temperature Water and its Role in Influencing Crack Growth Data,” Proc. of the Fourth Intl. Symp. on Environmental Degradation of Materials in Nuclear Power Systems-Water Reactors, D. Cubicciotti, ed, NACE International, Houston, TX, pp. 4.86–4.111 (1990).

106. Briant, C. L., and E. L. Hall, “The Microstructural Causes of Intergranular Corrosion of Alloys 82 and 182,” Corrosion, 43, 539–548 (1987).

107. Bamford, W. H., J. P. Foster, and R. S. Pathania, “An Investigation of Alloy 182 Stress Corrosion Cracking in Simulated PWR Environment”, Proc. of the Ninth Intl. Symp. on Environmental Degradation of Materials in Nuclear Power Systems-Water Reactors, F. P. Ford, S. M. Bruemmer, and G. S. Was, eds., The Minerals, Metals, and Materials Society, Warrendale, PA, pp. 279–294 (1999).

108. Bamford, W. H., J. P. Foster, K. R. Hsu, L. Tunon–Sanur, and A. McIlree, “Alloy 182 Weld Crack Growth, and its Impact on Service–Induced Cracking in Operating PWR Plant Piping,” Proc. Tenth Intl. Conf. on Environmental Degradation of Materials in Nuclear Power Systems-Water Reactors, NACE International, Houston, TX (2001).

109. Lindstrom, R., P. Lidar, and J. Lagerstrom, “Crack Growth of Alloy 182 in Simulated Primary Side PWR Environment,” Proc. of the 8th Intl. Symp. on Environmental Degradation of Materials in Nuclear Power Systems-Water Reactors, S. M. Bruemmer, ed., American Nuclear Society, La Grange Park, IL, pp. 422–429 (1997).

110. Le Hong, S., J. M. Boursier, C. Amzallag, and J. Daret, “Measurement of Stress Corrosion Cracking Growth Rates in Weld Alloy 182 in Primary Water of PWR,” Proc. Tenth Intl. Conf. on Environmental Degradation of Materials in Nuclear Power Systems-Water Reactors, NACE International, Houston, TX (2001).

111. Cassagne, T., D. Caron, J. Daret, and Y. Lefevre, “Stress Corrosion Crack Growth Rate Measurements in Alloys 600 and 182 in Primary Loops Under Constant Load,” Proc. of the Ninth Intl. Symp. on Environmental Degradation of Materials in Nuclear Power Systems-Water Reactors, F. P. Ford, S. M. Bruemmer, and G. S. Was, eds., The Minerals, Metals, and Materials Society, Warrendale, PA, pp. 217-224 (1999).

112. Magdowski, R., and M. Speidel, “Stress Corrosion Crack Growth of Weld Material Alloy 182 in Simulated PWR Environments,” Institute of Metallurgy, Swiss Federal Institute, Internal Report No. 226, Zurich (Jan. 2001).

113. Jacko, R. J., R. E. Gold, G. V. Rao, K. Koyama, and A. Kroes, “Results of Accelerated SCC Testing of Alloy 82, Alloy 182 and Alloy 52M Weld Metals,” presented at Vessel Penetration Inspection, Crack Growth and Repair Conference, Oct. 2, 2003, Gaithersburg, MD (2003).

114. Attanasio, S., J. V. Mullen, J. W. Wuthrich, W. W. Wilkening, and D. S. Morton, “Stress Corrosion Crack Growth Rates (SCCGRs) for Alloy 182 and 82 Welds,” presented at Vessel Penetration Inspection, Crack Growth and Repair Conference, Oct. 2, 2003, Gaithersburg, MD (2003).

NRC FORM 335
(9-2004)
NRCMD 3.7

U. S. NUCLEAR REGULATORY COMMISSION

BIBLIOGRAPHIC DATA SHEET

(See instructions on the reverse)

1. REPORT NUMBER

NUREG/CR–4667. Vol. 34
ANL—05/17

2. TITLE AND SUBTITLE

Environmentally Assisted Cracking in Light Water Reactors, Annual Report, January–December 2003

3. DATE REPORT PUBLISHED

MONTH	YEAR
May	2006

4. FIN OR GRANT NUMBER

Y6388

5. AUTHOR(S)

B. Alexandreanu, O. K. Chopra, H. M. Chung, E. E. Gruber, W. K. Soppet, R. W. Strain, and W. J. Shack

6. TYPE OF REPORT

Technical; Topical

7. PERIOD COVERED (Inclusive Dates)

8. PERFORMING ORGANIZATION – NAME AND ADDRESS *(If NRC, provide Division, Office or Region, U.S. Nuclear Regulatory Commission, and mailing address; if contractor, provide name and mailing address.)*

Argonne National Laboratory
9700 South Cass Avenue
Argonne, IL 60439

9. SPONSORING ORGANIZATION – NAME AND ADDRESS *(If NRC, type "Same as above": if contractor, provide NRC Division, Office or Region, U.S. Nuclear Regulatory Commission, and mailing address.)*

Division of Fuel, Engineering & Radiological Research
Office of Nuclear Regulatory Research
U.S. Nuclear Regulatory Commission
Washington, DC 20555–0001

10. SUPPLEMENTARY NOTES

W. H. Cullen, Jr., and C. E. Moyer, NRC Project Managers

11. ABSTRACT (200 words or less)

This report summarizes work performed by Argonne National Laboratory on fatigue and environmentally assisted cracking (EAC) in light water reactors (LWRs) from January to December 2002. Topics that have been investigated include: (a) environmental effects on fatigue crack initiation in carbon and low–alloy steels and austenitic stainless steels (SSs), (b) irradiation–assisted stress corrosion cracking (IASCC) of austenitic SSs in BWRs, (c) evaluation of causes and mechanisms of irradiation-assisted cracking of austenitic SS in PWRs, and (d) cracking in Ni–alloys and welds. Fatigue tests have been conducted on two heats of Type 304 SS under various material conditions to determine the effect of heat treatment on fatigue crack initiation in these steels in air and LWR environments. Slow-strain-rate tensile tests have been completed in high-purity 289°C water on steels irradiated to ≈3 dpa. The bulk S content provided a good correlation with the susceptibility to intergranular SCC in 289°C water. Crack growth tests were performed in BWR environments on SSs irradiated to 0.3 x 10^{21} n/cm^2 and on nonirradiated SS weld heat affected zone specimens. The irradiated specimen of Heat C3 showed very little enhancement of CGRs in high–DO water. Crack growth tests were completed on a Alloy 600 round robin specimen and a Alloy 182 weld specimen in simulated PWR water at 320°C. Under cyclic loading, the CGRs for the weld specimen were a factor of ≈5 higher than for Alloy 600 under the same loading conditions; little or no environmental enhancement was observed.

12. KEY WORDS/DESCRIPTORS *(List words or phrases that will assist researchers in locating this report.)*

Fatigue Crack Initiation
Crack Growth Rate
Irradiation–Assisted Stress Corrosion Cracking
Radiation–Induced Segregation
Stress Corrosion Cracking
Nickel Alloys

13. AVAILABILITY STATEMENT

unlimited

14. SECURITY CLASSIFICATION

(This Page)
unclassified

(This Report)
unclassified

15. NUMBER OF PAGES

139

16.PRICE